Equation of State Measurements on Iron Near the Melting Curve at Planetary Core Conditions by Shock and Ramp Compressions

S. C. Grant[1,2,*], T. Ao[2], C. T. Seagle[2], A. J. Porwitzky[2], J.-P. Davis[2], K. R. Cochrane[2], D. H. Dolan[2], J.-F. Lin[3,*], T. Ditmire[1], and A. C. Bernstein[1]

[1]Center for High Energy Density Science, The University of Texas at Austin, Austin, Texas 78712, USA.

[2]Sandia National Laboratories, Albuquerque, New Mexico 87185, USA.

[3] Department of Geological Sciences, Jackson School of Geosciences, University of Texas at Austin, Austin, Texas 78712, USA.

*Corresponding authors: Sean Grant (sgrant@utexas.edu), Jung-Fu Lin (afu@jsg.utexas.edu)

Key Points:

- We measure the pressure-density equation of state of ramp compressed iron near the melt line
- We benchmark a multi-phase SESAME equation of state with our data
- We note the range of planets which would contain a liquid outer core for certain temperature profiles based on planetary interior modeling

Abstract

The outer core of the Earth is composed primarily of liquid iron, and the inner core boundary is governed by the intersection of the melt line and the geotherm. While there are many studies on the thermodynamic equation of state for solid iron, the equation of state of liquid iron is relatively unexplored. We use dynamic compression to diagnose the high-pressure liquid equation of state of iron by utilizing the shock-ramp capability at Sandia National Laboratories' Z-Machine. This technique enables measurements of material states off the Hugoniot by initially shocking samples and subsequently driving a further, shockless compression. Planetary studies benefit greatly from isentropic, off-Hugoniot experiments since they can cover pressure-temperature (P-T) conditions that are close to adiabatic profiles found in planetary interiors. We used this method to drive iron to P-T conditions similar to those of the Earth's outer-inner core boundary, along an elevated-temperature isentrope in the liquid from 275 GPa to 400 GPa. We derive the equation of state using a hybrid backward integration – forward Lagrangian technique on particle velocity traces to determine the pressure-density history of the sample. Our results are in excellent agreement with SESAME 92141, a previously published equation of state table. With our data and previous experimental data on liquid iron we provide new information on the iron melting line and derive new parameters for a Vinet-based equation of state. The table and our parameterized equation of state are applied to provide an updated means of modeling the pressure, mass, and density of liquid iron cores in exoplanetary interiors.

1 Introduction

The core conditions of terrestrial planets between one and ten Earth masses, those most likely to maintain a life-protecting magnetic field, range from a few 100 GPa and several thousand Kelvin to several TPa and over ten thousand Kelvin (Wagner et al., 2011). Because of the great uncertainty of constituent materials at these P-T conditions, we lack understanding of the history and dynamics of the interior of the Earth and other planets, in our solar system and beyond. Astronomers have used ground- and space-based telescopes to discover planets by detecting the transit of a planet across its star, often measuring the mass and radius of these newly discovered planets (Batalha et al., 2011; Gillion et al., 2017; Léger et al., 2009; Marcy et al., 2014; Ricker et al., 2014). The equations of state (EOS) of the constituent materials used to determine the likely structure and condition of these planets (Fortney et al., 2007; Léger et al., 2011; Rogers & Seager, 2010; Sotin et al., 2007; Swift et al., 2012; Valencia et al., 2006) are often derived from extrapolations of static and shock measurements. For this reason, high-pressure EOS experiments are necessary to advance our understanding in these areas (Valencia et al., 2009).

Of particular interest on the subject is to study iron with relevance to the metallic cores of planetary interiors. Recent theoretical and experimental findings provide rich information yet also leave open questions regarding iron's melting point, thermal conductivity, and off-Hugoniot EOS (Buffett, 2000; Konopkova et al., 2016; Morard et al., 2018; Ohta et al., 2016; Soubiran & Militzer, 2018). Terrestrial planetary cores are largely made of iron with a small amount of impurities, and potentially contain both the liquid and solid phases. The inner core boundary separating the liquid outer core and the solid inner core is defined by the intersection of the planet's adiabat and the melt line of the iron alloy found in the core. The presence of a liquid outer core is important for a life-supporting planet – the magnetic field which protects our planet is thought to be maintained by the geodynamo, which is driven by the churning of the conductive liquid in the outer core powered by thermal, chemical, and possibly radioactive energy sources (Buffett, 2000; Busse, 1976). As a planet cools, the solid inner core grows and the liquid outer core shrinks so latent heat and light elements are released into the liquid outer core to power the geodynamo. This thermal cooling will eventually lead to the core becoming completely solid, ending the generation of the magnetic fields. This subject on thermal cooling in turn has generated great interest in knowing the melt line and EOS of iron near the melt line. There is a wealth of experimental results for solid iron taken statically with diamond anvil cells (Dewaele et al., 2006; Fei et al., 2016), through shock experiments (Brown & McQueen, 1986; Nguyen & Holmes, 2004; Ping et al., 2013), with quasi-isentropic compression starting at ambient or high pressures (Bastea et al., 2009; Smith et al., 2018; Wang et al., 2013), and by studies off the principal Hugoniot through the shock of preheated samples (Chen & Ahrens, 1998). There are also theoretical works that span a wide range of physical parameters (Alfe et al., 2002; Sha & Cohen, 2010; Sjostrom & Crockett, 2018). Shock experiments can reach the liquid state, but are often restricted to a specific locus of P-T conditions, known as the Hugoniot, such that specific P-T conditions of interest to planetary cores could not be accessed by traditional means. Meanwhile, x-ray diffraction, one of the common techniques used in static compression, is difficult to be used to investigate the EOS of liquid iron at such P-T extremes. This has led to relatively little experimental work on liquid iron reported thus far (Morard et al., 2013; Sanloup et al., 2011), particularly at P-T conditions relevant to Earth's core, leaving theoretical researchers with few options for comparison and benchmarking.

Figure 1a shows an experimentally estimated (Brown & McQueen, 1986) and a calculated (Sjostrom & Crockett, 2018) principal Hugoniot, a principal isentrope (Wang et al., 2013) for iron, the iron melt line (Anzellini et al., 2013), the core geotherm (Stacey & Davis, 2008), and a calculated elevated isentrope near a previously explored shock-ramp experiment (Wang et al., 2013). These experiments covered different P-T conditions and there are some discrepancies among the different results for the melt line; for a recent update on this topic see, for example, Sinmyo et al. (2019). We reference the melt curve by Anzellini et al. (2013) as it is commonly used and their curve agrees well with past dynamic experiments (Brown & McQueen, 1986; Nguyen & Holmes, 2004) and the recent shock experimental work by Li et al. (2020), for which some data points are included in Figure 1. The calculated principal Hugoniot in Figure 1a is from SESAME 92141, a tabulated multi-phase EOS that covers a broad range of extreme conditions. The table is generated using a combination of experimental and theoretical results, but experimental benchmarking at planetary core P-T conditions would be extremely useful since these experimental results were lacking when the table was created. The geotherm for the liquid outer core lies below the pure iron melt line because this melt line does not include the effect of light elements in the Earth's core which would depress the melt line by hundreds of degrees relative to pure iron (Zhang et al., 2018). To visualize this, we have included a melt line which includes Fe alloyed with a single light element, silicon (Fe-8wt%Si) (Zhang et al., 2018). Even this is a representative melt line, as the Earth's core is likely to contain other light elements which would depress the melt line further (Morard et al., 2014). In comparison to the geotherm, the principal isentrope of iron is too cold and the principal Hugoniot is too hot, rapidly reaching very high temperatures. Isentropes are particularly relevant in a planetary context; many layers of a planet have an adiabatic temperature profile resulting from vigorous internal convections (Stacey & Davis, 2008), and isentropic or quasi-isentropic experiments mimic this thermodynamic path very well. Ramp compression of a solid involves stress heating, which leads to a higher temperature thermodynamic path than an isentrope, so we refer to ramp compression of solids as quasi-isentropic. Ramp compression of a liquid only has minimal heating from viscosity, so we refer to this as isentropic. To reach the otherwise difficult inner core boundary (ICB) P-T conditions and to achieve the elevated-temperature isentropes that are most appropriate for planetary studies we employ the shock-ramp technique. We designed an off-Hugoniot ramp compression experiment starting from a 270 GPa shock to achieve ICB conditions, shown in Figure 1a. We also show a second potential experiment design to access the liquid phase through a shock-release path, such an experiment can access the liquid state from a lower shock pressure than a shock-ramp experiment. Figure 1b shows the calculated Hugoniot and simulated elevated isentrope in pressure and density, compared to the results of two previous shock-ramp experiments in the solid phase (Smith et al., 2018; Wang et al., 2013). The results by Smith et al. (2018) were reduced to a principal isentrope, while the results by Wang et al. (2013) are measurements of stress versus density.

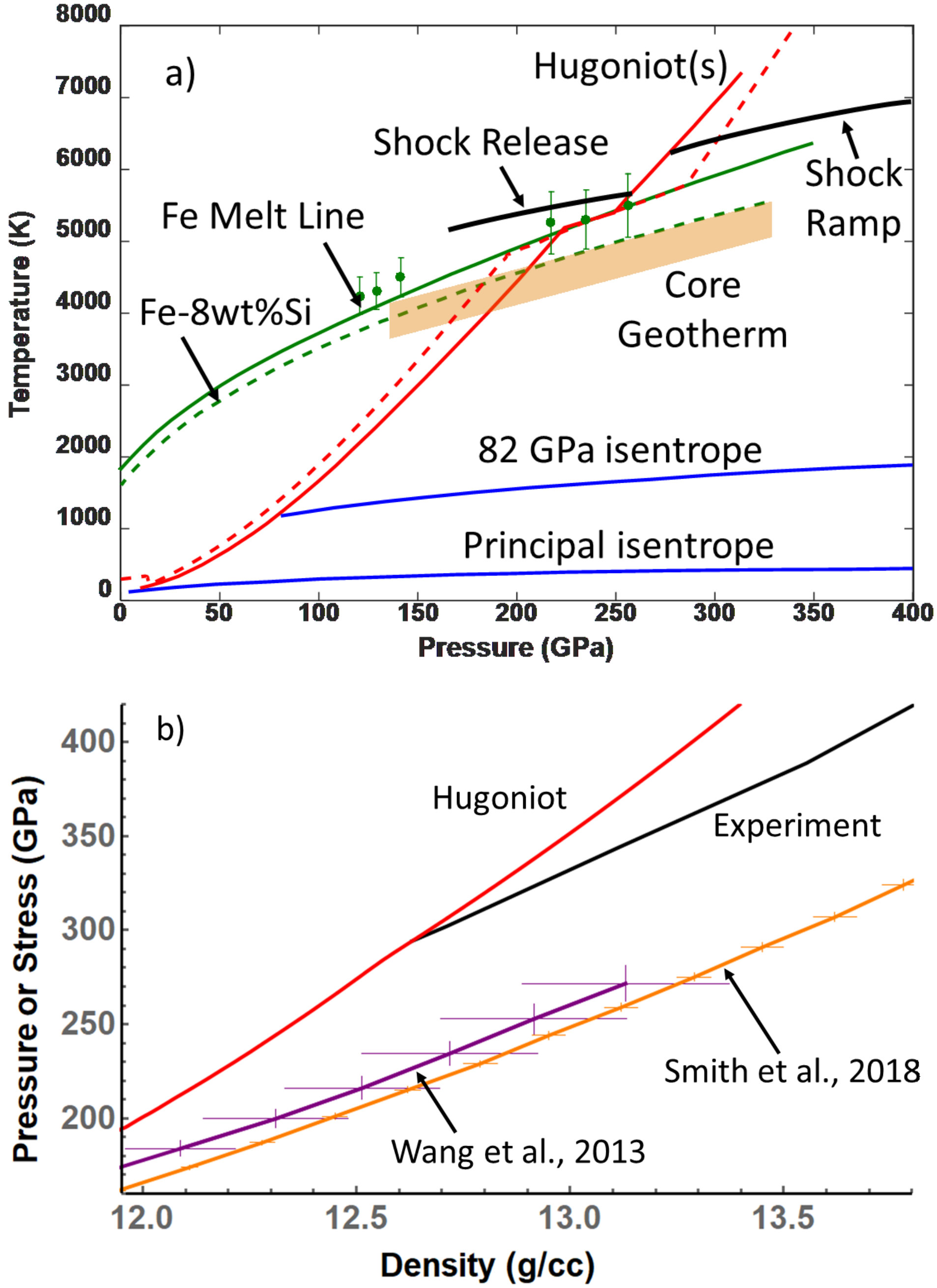

Figure 1. P-T conditions in Earth's core and shock experiments. a) Our simulated experimental paths (black) are compared with the melt line for iron (Anzellini et al., 2013) (green) and Fe-8wt%Si (Zhang et al., 2018) (green-dashed), Earth's core geotherm (Stacey & Davis, 2008) (orange), experimentally estimated (Brown & McQueen, 1986) (red) and calculated (Sjostrom & Crockett, 2018) (red-dashed) principal Hugoniot, principal isentrope (Wang et al., 2013) (blue), and calculated 82 GPa shock ramp elevated isentrope (Wang et al., 2013) for iron. We have also included the latest experimental data for the iron melt line from Li et al. (2020) (green circles). **b)** The pressure-density paths of the same calculated Hugoniot (red), simulated

experiment (black), and the results from two solid off-Hugoniot ramp-compression experiments, stress-density results starting from 82 GPa (Wang et al., 2013) (purple) and reduced principal isentrope pressure-density results (Smith et al., 2018) (orange).

In this work, we look at the high-pressure off-Hugoniot EOS of pure iron into the liquid state in order to better model density profiles of terrestrial planetary cores. Using the Sandia Z-Machine (Savage et al., 2007), we have obtained ramp compression measurements which were analyzed using an iterative backward integration – forward Lagrangian technique (Davis, 2006; Maw, 2004; Rothman et al., 2005; Rothman & Maw, 2006; Seagle & Porwitzky, 2018). Our results are compared with previous EOS results (Sjostrom & Crockett, 2018; Smith et al., 2018; Wang et al., 2013) and modeled to derive ultrahigh P-T EOS parameters of liquid iron. Finally, these results are used to build a radial planetary model and applied to planetary implications. The direction of future works in the context of planetary science applications is also discussed.

2 Materials and Methods

2.1 Experimental methods

Shock experiments were performed at Sandia National Laboratories' Z-Machine, a pulsed power facility capable of delivering up to 26 MA of current. We use the Z-Machine in the 'strip-line' configuration (Lemke, 2011), a schematic of which is shown in Figure 2. The machine delivers current through two parallel aluminum panels creating an outward electromagnetic force that symmetrically drives the panels apart. There are two primary methods of using this configuration to create high pressures in a sample. The first method is quasi-isentropic compression, generally referred to as 'ramp' compression (Ao et al., 2009; Hall et al., 2001). The samples are attached directly to the panel and the current pulse is designed to increase over the course of the experiment. As the panels are forced apart by the current pulse, the sample experiences a shockless compression which drives the samples to high pressures while maintaining relatively low temperatures. The second common technique is shock compression. There is a 0.6 mm gap between the samples and the panel, referred to as the flight gap, so that the current pulse can accelerate the panel to and hold at a designed ballistic impact speed before impacting the sample. This creates a shock which drives the sample to a state on the Hugoniot (Lemke et al., 2005).

While these are two of the common configurations, the Z-Machine can combine these two methods to reach a wider variety of P-T conditions (Seagle et al., 2013). This is generally referred as 'shock-ramp'. There is a flight gap between the panel and samples, as in a shock experiment, but the current pulse is shaped such that after impact the panel continues to drive the sample to higher pressures via shockless compression. Ideally, the flyer has little to no acceleration when it impacts the sample, providing a consistent, steady shock state prior to the subsequent ramp compression. This technique allows us to drive samples along off-Hugoniot isentrope paths, greatly expanding the P-T space that can be explored.

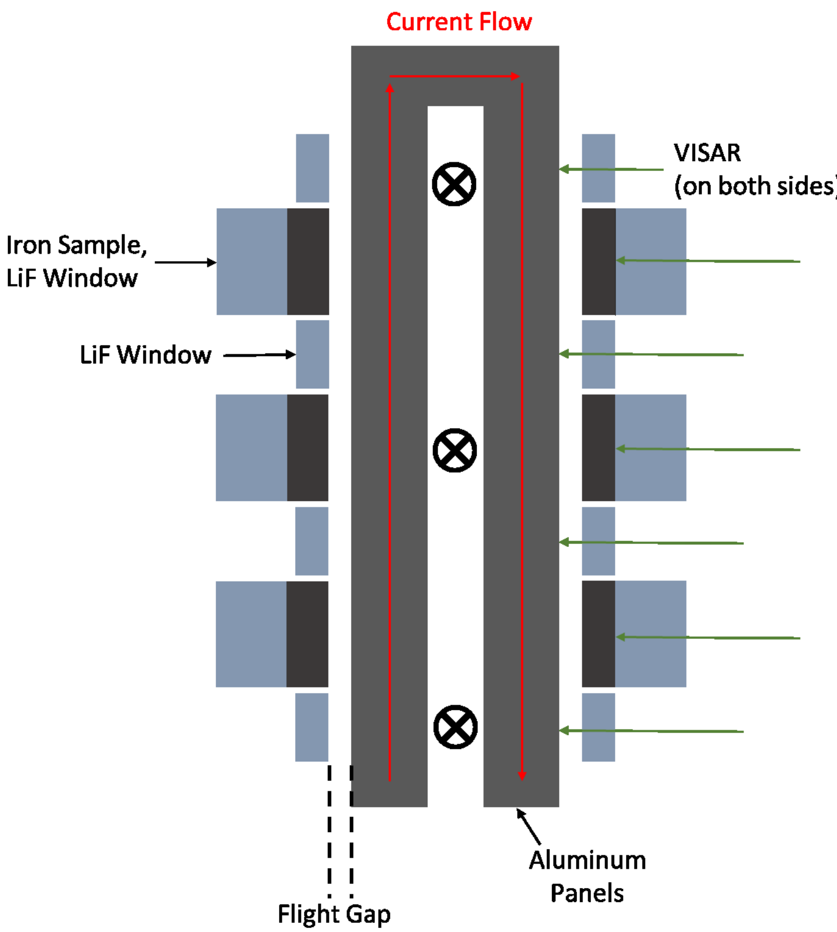

Figure 2. Schematic cross-sectional view of the panel configuration for Z-Machine experiments. The VISAR diagnostic is present on both panels, but only one side is shown here to minimize visual clutter. The red lines with arrows show the current flow through aluminum panels, and the cross-circles show the magnetic field in-between them.

The scientific objectives of this experiment to measure the EOS of iron at ICB conditions push the limit of the Z-Machine's capabilities. The high initial shock condition necessary to shock-melt the iron upon impact is larger than that in any previous shock-ramp type experiments. This requires that the pre-impact velocity held in the pulse shape occurs at relatively high currents, and that the flight gap be relatively large, to allow ample space for the panel to accelerate up to speed. Since an increased separation of the panels increases the inductance of the load, these two factors lead to the need for designing the structure of the pulse to steepen at a time when the load inductance is unusually high and the machine is already driving a large current. This results in higher than expected current loss during the ramp compression stage of the experiment. These experimental constraints prevented us from reaching higher pressures along the isentropes explored in this work. Further details and discussion of possible implications and insights from these considerations can be found elsewhere (Porwitzky et al., 2019).

Figure 2 shows the sample arrangement. There are six sample locations on each experiment, three on each of the panels. Each sample is a 7.3 mm tall by 8 mm wide rectangular piece of iron between 0.9 and 1.8 mm thick. The samples are 99.99+% purity polycrystalline bulk iron with a density of 7.836 g/cc. Every sample has a 2.5 mm thick lithium fluoride (LiF) window glued to it for better impedance matching than vacuum. This maintains a higher-pressure release state and improves surface integrity at the rear surface being probed by the optical diagnostics.

The two panels are driven apart symmetrically, so the two samples across from each other, such as the top sample on each of the two panels, should experience the same drive conditions; we refer to these samples as a sample pair. Above and below every sample is a small LiF window, called a witness window, for providing a direct line of sight to the panel itself. We use these witness windows to determine when the panel reaches the impact plane via a jump in the velocimetry signal. While sample pairs experience the same drive, there are small deviations along the panel from top to bottom due to higher current densities near the shorting cap at the top of the panels and lower current densities at the bottom of the panels. These witness windows enable us to average the impact time and speed of the panel above and below each sample to estimate the on-sample values. This averaging results in a maximum error of 0.5% in impact time and speed.

We use a Velocity Interferometer System for Any Reflector (VISAR) diagnostic to measure the particle velocity at the iron-LiF interfaces as well as the aluminum flyer velocity at locations adjacent to the samples (Barker & Hollenbach, 1972; Dolan, 2006). One VISAR point is used for each sample as well as the panel through every witness window. This VISAR utilizes 532 nm light, delivered to and received from the sample by a bare two-fiber probe with 200 μm fiber cores. The system probes a spot-size of approximately 100 μm on the sample. We use vpf (velocity per fringe) settings ranging between 0.4 and 1.1 km/s/f with a temporal resolution of 300 ps. The apparent particle velocity measured by the VISAR at the sample locations is corrected to the actual interface velocity via the non-linear LiF window correction proposed by Rigg et al. (2014).

There are three main considerations when choosing the thicknesses of the samples in the sample pairs. First, ramp waves would steepen and eventually become shock waves as they travel through a sample. If a sample is too thick, then the ramp drive will become partially shocked by the time it reaches the measured interface, which degrades the EOS analysis. Second, when the release wave from the window interface of the thinner sample in a pair makes it back to the front drive surface, the drive condition experienced by that sample no longer matches the other sample in the pair. This breaks one of the assumptions of the analysis, so results beyond this point are not valid. It is important to keep samples from being too thin as this will lead to the reverberation invalidating our data at an earlier time. Finally, increasing the difference in thickness between the two samples reduces the error in the EOS parameters since the error in the sample thicknesses is divided by the thickness difference in the error analysis. The thickness of the thin sample is therefore chosen to optimize maximum pressure while ensuring a low error. In our first experiment, for example, we chose sample thicknesses such that one pair is optimized to reach higher pressure (1.0 mm and 1.2 mm), and another pair is optimized for lower error (0.9 mm and 1.2 mm).

2.2 Data analysis

We perform an iterative backward integration – forward Lagrangian analysis on the velocimetry data to obtain the relationship between pressure, density, sound speed, and particle velocity for iron along the isentropes we explored (Hayes, 2001; Maw, 2004; Rothman et al., 2005; Rothman & Maw, 2006; Seagle et al., 2016; Seagle & Porwitzky, 2018). We analyze each of the sample pairs independently since this process requires multiple targets of different thicknesses undergoing the same loading conditions. We backwards-integrate the velocity profile at the sample-window interface using the Lagrangian hydrodynamic equation of motion and mass conservation:

$$\frac{\delta[P(\rho)]}{\delta x} = -\rho_0 \frac{\delta u}{\delta t} \quad Eq. 1$$

$$\frac{1}{\rho_0}\frac{\delta u}{\delta x} = \frac{\delta\left[\frac{1}{\rho}\right]}{\delta t} \quad Eq. 2$$

to get the density-particle velocity profile of the ramp pulse at the sample's drive interface. In Equations 1 & 2, P is pressure – we shock melt the iron in these experiments, so we use pressure instead of stress, which would have to be used for a solid experiment – u is particle velocity, ρ is density, t is time, and x is Lagrangian position.

Lacking other information, this backwards integration will assume that a shockwave seen at the sample-window interface was created via the steepening of a ramp-wave leading up to this surface. Because the shock wave originates at the drive surface, it is used as a boundary condition in the analysis. Since the shock front boundary can be a complicated function in x *and* t space, it is convenient to employ a change of variables. As done in Seagle and Porwitzky (2018), we use the new space and time variables $q = q(x)$ and $\tau = \tau(x, t)$, which yield the new hydrodynamic equations:

$$\frac{\delta[P(\rho)]}{\delta q}\frac{\delta q}{\delta x} + \frac{\delta[P(\rho)]}{\delta \tau}\frac{\delta \tau}{\delta x} = -\rho_0 \frac{\delta u}{\delta \tau}\frac{\delta \tau}{\delta t} \quad Eq. 3$$

$$\frac{1}{\rho_0}\left[\frac{\delta u}{\delta q}\frac{\delta q}{\delta x} + \frac{\delta u}{\delta \tau}\frac{\delta \tau}{\delta x}\right] = \frac{\delta\left[\frac{1}{\rho}\right]}{\delta t}\frac{\delta \tau}{\delta t} \quad Eq. 4$$

A good choice of normalized equations for these variables is $q = x/x_T$ and $\tau = \frac{[x - x_S(t)]}{[x - x_S(t_f)]}$, where x_S is the Lagrangian position of the shock front as a function of time, x_T is the thickness of the sample, and t_f is the final time of interest. This choice for the variable change ensures that the τ=0 boundary follows the shock front. When the shock wave is steady, the whole bulk of the sample is constrained to the isentrope containing the Hugoniot point associated with this shock state. The pressure depends only on the density for such cases, and this was often a reasonable assumption in previous works. However, if the shock state is not steady, then each Lagrangian position is constrained to the isentrope that contains the Hugoniot point experienced at that Lagrangian position. This means that the sample experiences the range of isentropes that contain the range of Hugoniot points experienced within that sample, and an accurate representation of the $P(\rho)$ function should include an explicit dependence on x, and thus q. We will represent this as $P(\rho,q)$ from now on, and also note that ρ implicitly depends on both q and τ. With these changes, the hydrodynamic equations take the form:

$$\frac{\delta[P(\rho,q)]}{\delta q}\frac{1}{x_T}+\frac{\delta[P(\rho,q)]}{\delta\tau}\frac{(1-\tau)}{\left(qx_T-x_S(t_f)\right)}=\rho_0\frac{\delta u}{\delta\tau}\frac{U_s(\tau,q)}{\left(qx_T-x_S(t_f)\right)}\quad Eq.5$$

$$\frac{1}{\rho_0}\left[\frac{1}{x_T}\frac{\delta u}{\delta q}+\frac{\delta u}{\delta\tau}\frac{(1-\tau)}{\left(qx_T-x_S(t_f)\right)}\right]=-\frac{\delta\left[\frac{1}{\rho}\right]}{\delta t}\frac{U_s(\tau,q)}{\left(qx_T-x_S(t_f)\right)}\;,\qquad Eq.6$$

where U_S is the shock speed, or $\delta x_S(t)/\delta t$.

Deviations from the ideal pulse profile in our experiments led to non-steady shock waves, so we implement this variable-shock wave analysis. Given that we only have three reference points for this shock wave – the impact interface, and the two sample-window surfaces – we fit the shock speed as a quadratic in space.

To complete the analysis, appropriate boundary conditions also need to be defined. The particle velocity and density of the sample for both the measured sample-window interface and the shock front are used for the following boundary conditions:

$$u(1,\tau)=u_b(\tau)\quad Eq.7$$

$$u(q,0)=\begin{cases}u_p^H(q)\ if\ q<1\\ u_b(0)\ \ if\ q=1\end{cases}\quad Eq.8$$

$$\rho(1,\tau)=\rho_b(\tau)$$

$$\rho(q,0)=\begin{cases}\rho^H(q)\ if\ q<1\\ \rho_b(0)\ if\ q=1\end{cases},\quad Eq.9$$

where u_b and ρ_b are the particle velocity and density, respectively, measured at the sample-window interface, and the H superscript indicates the Hugoniot state along the shock front. It should be noted that the Hugoniot state has a dependence on q because of the non-steady shock state. The Hugoniot states are established from the SESAME 92141 iron EOS table (Sjostrom & Crockett, 2018). These boundary conditions state that the q=1 boundary or the sample-window interface must match our measured observations, and that the τ=0 boundary matches the shock front.

The SESAME 7271v3 EOS for LiF (Davis et al., 2016) is used to determine ρ_b based on the measured u_b, while SESAME 3700 is used for the aluminum EOS (Kerley, 1987). The EOS for iron, the EOS for the aluminum panel, and the panel velocity measurements taken above and below each sample establish the initial Hugoniot state and impact time at the drive surface. The impact time at the sample surface is calculated as the average of the impact times present in the adjacent witness window VISAR traces.

From the calculated drive conditions, $u(0,t)$ and $\rho(0,t)$, the in-situ particle velocities for the sample-window interface locations are calculated using the method of characteristics (Zel'Dovich & Raizer, 2002). In this analysis, the sound speed is calculated from the input EOS to propagate the drive profile forward. These are the values that would exist if the sample was infinitely thick and there were no release waves interacting with the drive. With these in-situ values, a standard Lagrangian sound speed analysis is then performed to calculate sound speed as a function of particle velocity via:

$$C_L(u_p) = \frac{\Delta x}{\Delta t(u_p)}, \quad Eq. 10$$

where $\Delta t(u_p)$ is the time difference between a particle velocity at the thicker location and the same particle velocity at the thinner location. In the case of a release before the ramp compression, the sound speed is calculated starting at the beginning of the final ramp compression. The pressure and density as a function of particle velocity are found through these two equations, based on the Riemann invariants:

$$\frac{1}{\rho(u_p)} = \frac{1}{\rho_s} - \int_{u_{ps}}^{u_p} \frac{du_p}{\rho_0 C_L} \quad Eq. 11$$

$$P(u_p) = P_s + \int_{u_{ps}}^{u_p} \rho_0 C_L du_p . \quad Eq. 12$$

where the *s* subscript indicates the shock state. Since there are a range of shock states within the sample, we have chosen to use the drive shock state as the referenced shock state for these equations. Uncertainties associated with choosing this reference state are discussed and visualized with the presentation of the data. This creates a new pressure-density EOS for the sample. The new EOS, which covers the compression states of the experiment, is fitted to a Mie-Gruneisen EOS model and extrapolated down in pressure to include the release conditions also found within the experiment. The whole process is repeated, using this new iron EOS to replace our initial input parameters, and this iteration continues until the output EOS converges to a solution.

The modifications to the analysis detailed here are tested against simulated data generated using an EOS table, and the analysis is able to reproduce the pressure and density values in the simulation using the particle velocity traces extracted from the simulation at the sample-window interface. These simulations had a similar ramp structure and non-steady shock front to those in our experiments.

3 Equation of state data

Two experiments were performed on the Z-Machine, shot Z3155, and a second experiment, shot Z3339, that had more current loss than shot Z3155. The initial shock state in the iron was 270 and 265 ± 1 GPa, for shots Z3155 and Z3339, respectively. Shot Z3155 experienced a slight growing shock through the sample, reaching an estimated shock pressure of about 285 GPa. The subsequent ramp in shot Z3155 drove the iron pressure to about 450 GPa. The analysis here only holds up to the thinnest sample for a given sample pair, so our analysis reaches a peak pressure of 398 GPa. Shot Z3339 had enough current loss that the sample experienced a decaying shock and slight release before the ramp, instead of the ideal steady shock-hold. This loss resulted in the ramp starting from 220 GPa, and only reaching ~375 GPa. This creates a ramp path which covers a range from a path releasing into the liquid phase from a shock state near the completion of melting (Nguyen and Holmes, 2004), akin to the shock-release presented in Figure 1, to a release from a shock state which is only just beginning to melt. This means that parts of the samples in Z3339 are possibly being ramp compressed from a mixed phase state. Table 1 provides an overview of the shot details. The large decaying shock wave in shot Z3339 requires that we use the non-steady shock wave formulation of the analysis for accuracy. While we present our stress data as pressure because the samples are initially shocked into a liquid state, we note that this equality could be subject to error since the phase of our samples is not definitively liquid throughout the depth of the sample.

	Shot Z3155		**Shot Z3339**		
	Bottom Pair	**Middle Pair**	**Bottom Pair**	**Middle Pair**	**Top Pair**
Thick Sample Thickness (mm)	1.2041(2)	1.1925(2)	1.8032(2)	1.6898(2)	1.5934(2)
Thin Sample Thickness (mm)	0.9089(2)	1.0065(2)	1.2531(2)	1.2433(2)	1.2548(2)
Impact Shock (GPa)	270.4 ± 1.0	277.8 ± 1.0	265.3 ± 1.0	272.7 ± 1.0	275.9 ± 1.0
Estimated Maximum Shock (GPa)	286	286	265	273	276
Estimated Minimum Shock (GPa)	270	278	226	234	249
Minimum Ramp (GPa)	282 ± 5	284 ± 5	219 ± 3.5	217 ± 3.5	228 ± 3.5
Maximum Ramp (GPa)	365 ± 10	390 ± 17	345 ± 6.5	363 ± 8.9	372.5 ± 10.8

Table 1. Shot details for all experiments presented. Estimated maximum and minimum shock states are based on the quadratically fitted variable shock states with sample depth. Minimum and maximum ramp values shown represent the range of values extracted from the analysis, not the range of states experienced by the sample as the analysis does not always extend to the peak of the ramp compression.

The impact time and shock state were determined by the VISAR traces of the flyer through the LiF witness windows above and below each sample. Figure 3 shows the VISAR traces adjacent to the middle sample in Z3155. The fringe jump matching at impact was not calculated as we are only interested in the time of impact, indicated by the time of this fringe jump, and the velocity of the flyer just prior. Example VISAR traces of the sample-window interface from shot Z3155 are shown in Figure 4a, and traces from shot Z3339 are shown in Figure 4b to illustrate the partial release where the decreasing velocity after shock breakout is noted. The top pair of samples in shot Z3155 did not return quality velocity traces, so we have not included those data in any part of our results; all sample pairs from shot Z3339 are used. Figure 5 shows the density profile at the drive surface calculated by backwards-integrating the data in Figure 4a. The uncertainties in Figure 5 are a combination of the uncertainty in density from our completed iterative analysis as well as the uncertainty associated with the compression/release path leading up to the final ramp compression, which starts around 57 ns in the figure. We indicate the point at which the release wave from the sample-window interface reaches the drive surface of the thin sample. This is the point at which the analysis breaks down.

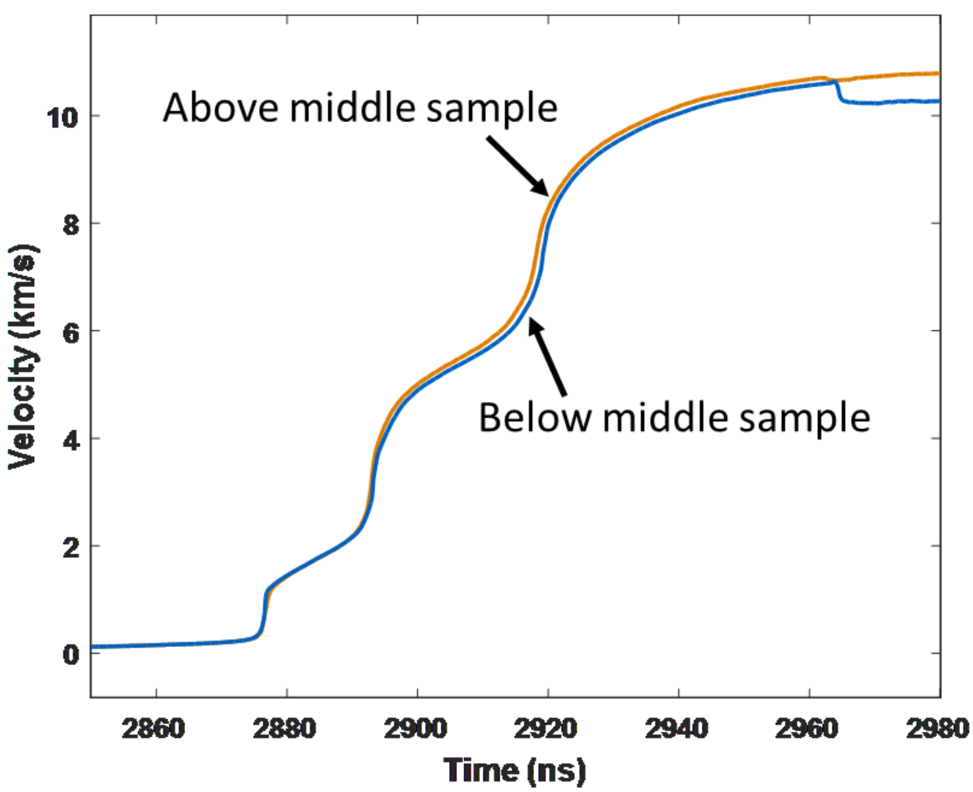

Figure 3. VISAR traces of the flyer from the witness window locations above and below one of the middle samples in Z3155. The flyer impacts the LiF witness windows at approximately 2964 ns. The number of fringes in this jump was not calculated, as the velocity beyond the impact time is not important for our results. The error in the VISAR traces is approximately 10 m/s and is not shown in these plots as it is comparable to the thickness of the lines.

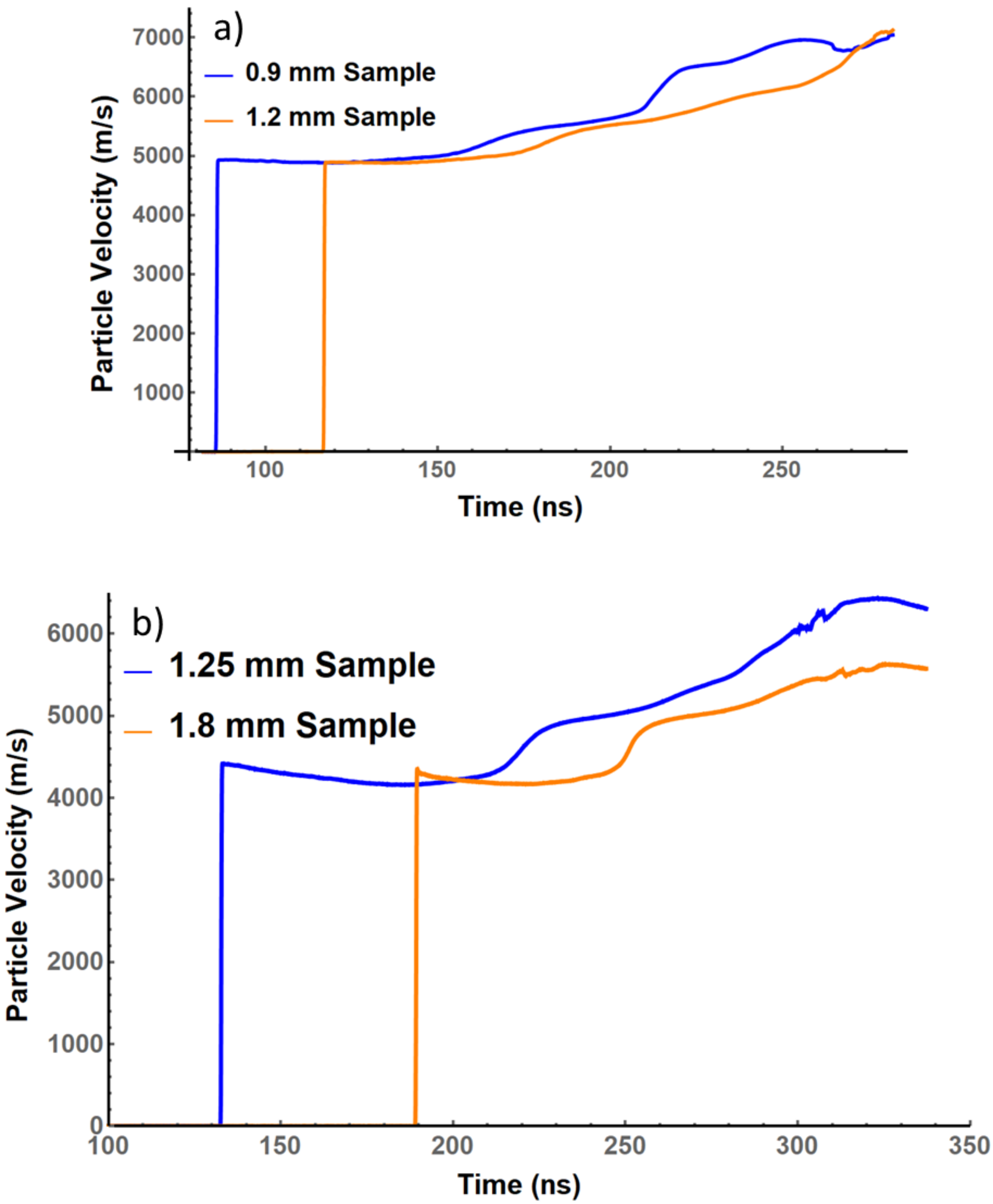

Figure 4. VISAR results from the sample-window interface for the bottom sample pair on **a)** shot Z3155 and **b)** shot Z3339. The time is shifted such that impact occurs at time zero. The error in the VISAR traces is approximately 10 m/s and is not shown in these plots as it is comparable to the thickness of the lines.

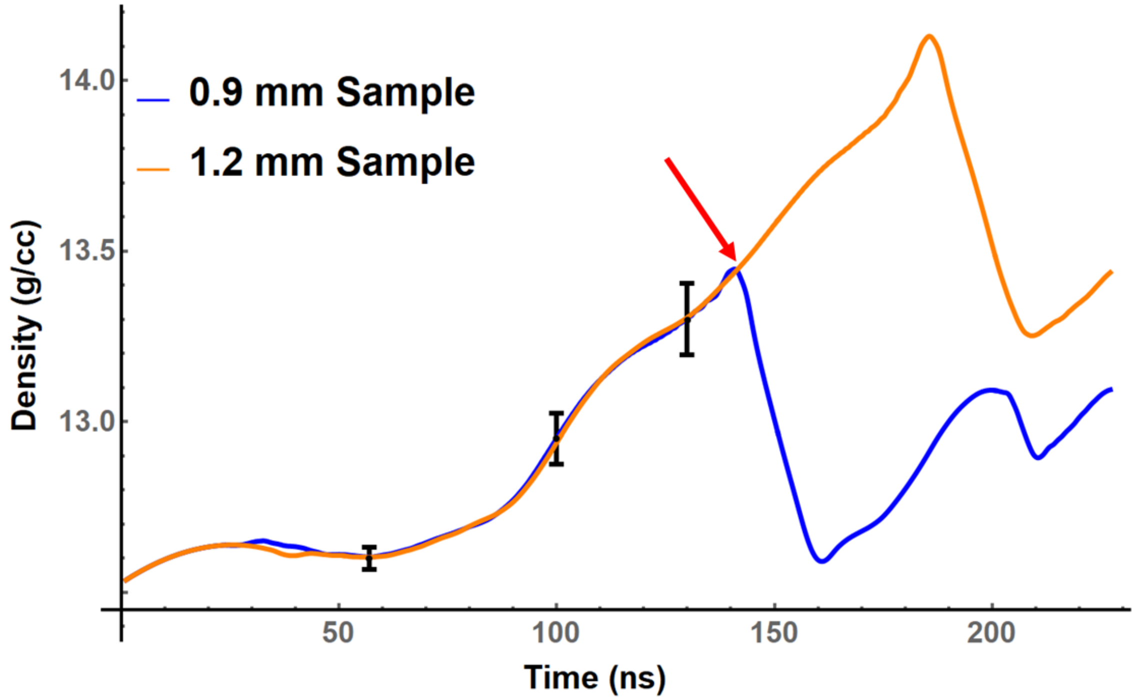

Figure 5. Density profile at the drive surface from the bottom pair samples on shot Z3155 derived from the backward integration of the sample-window interface measurement. The release reaching the drive surface for the thin sample is indicated by the red arrow. The same data set is also shown in Figure 3a.

The combined sound speed results are shown in Figure 6, and the individual pressure-density results are shown in Figure 7. The uncertainties in these results have been split into two separate considerations. The first error bounds, indicated by dashed lines in the Figure 6 and 7, result from propagation of uncertainty in the sample thickness (±0.2 μm) and the velocity traces (±10 m/s in velocity and ±300 ps in time). These uncertainties propagate into the sound speed and subsequent pressure-density calculations in the same manner as described in Rothman et al. (2005). The second uncertainty consideration results from pinning the start of the ramp compression. Equations 11 and 12 are used to integrate the EOS results from the sound speed starting at the base of the ramp compression. In a ramp-compression experiment this pinning point is typically ambient conditions, and is known very precisely. However, in an ideal shock-ramp experiment, this pinning point is the shock state, and is known with the same uncertainty as the obtained shock state. For our experiments here, we have the more complicated situation of a variable shock state followed by some ramp and/or release prior to the final ramp compression. Therefore, the pinning uncertainty is assigned using both the range of shock states in the experiment, shown in Table 1, and an estimation of the uncertainty in the initial ramp/release paths prior to the final ramp compression. The latter is based on an extrapolation of our own results. This uncertainty is indicated at the start of the curves by vertical tick marks. Shot Z3339 has smaller error in the ramp path than shot Z3155 because the thick samples are close to 0.5 mm thicker than in shot Z3155, creating a larger thickness difference between the thick and thin samples. We made this adjustment after the first experiments revealed that the ramp profiles in the samples are not close to shocking up – one of the main limitations on the thickness of the thick samples.

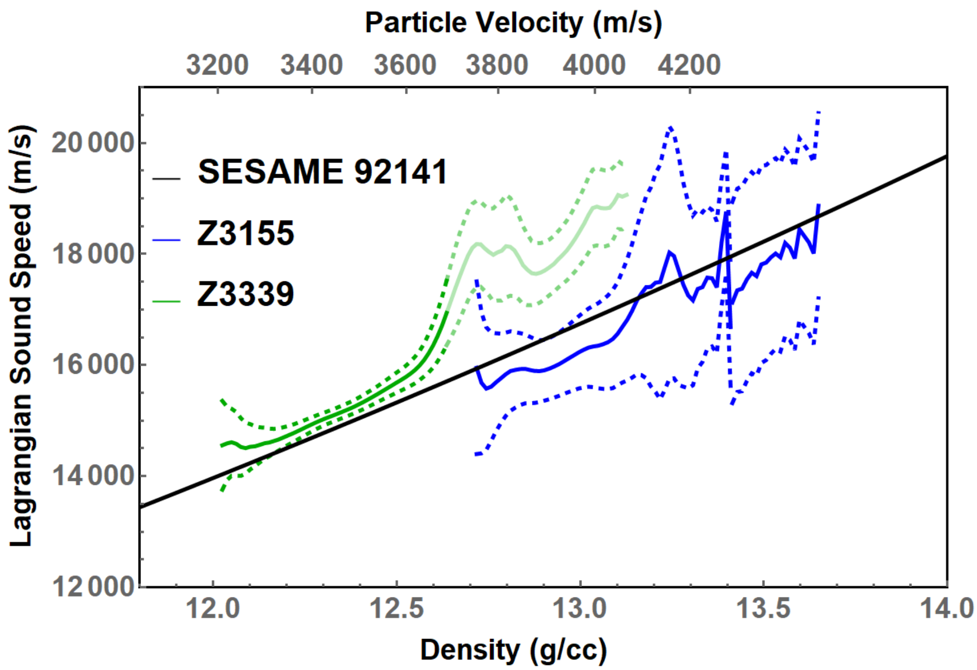

Figure 6. Lagrangian sound speed as a function of density and particle velocity for both shot Z3155 and shot Z3339. Traces are averaged over all available sample pairs. The non-converging data in Z3339 are de-emphasized by lightening.

The final combined pressure-density results from shot Z3155, including both the bottom and middle sample pairs, and the final combined traces for shot Z3339, including all three sample pairs, are shown in Figure 8. These are compared with the multi-phase iron SESAME 92141 EOS isentrope curves extracted from their respective Hugoniot points. Below 360 GPa, or 13.4 g/cc, the shot Z3155 trace is a combination of the two sample pairs, with error combined in quadrature, and above this point the trace is solely from the high-pressure sample pair. The shot Z3339 trace is a combination of all three sample pairs. The data generally agree well with the reference EOS. We also show the pressure-density paths explored by previous experiments on solid iron (Smith et al., 2018; Wang et al., 2013). We have an error of ~6 GPa at 13.0 g/cc density for the shot Z3155 data, compared with an estimated error of ~30 GPa for extrapolations from room-temperature static experiments (Smith et al., 2018).

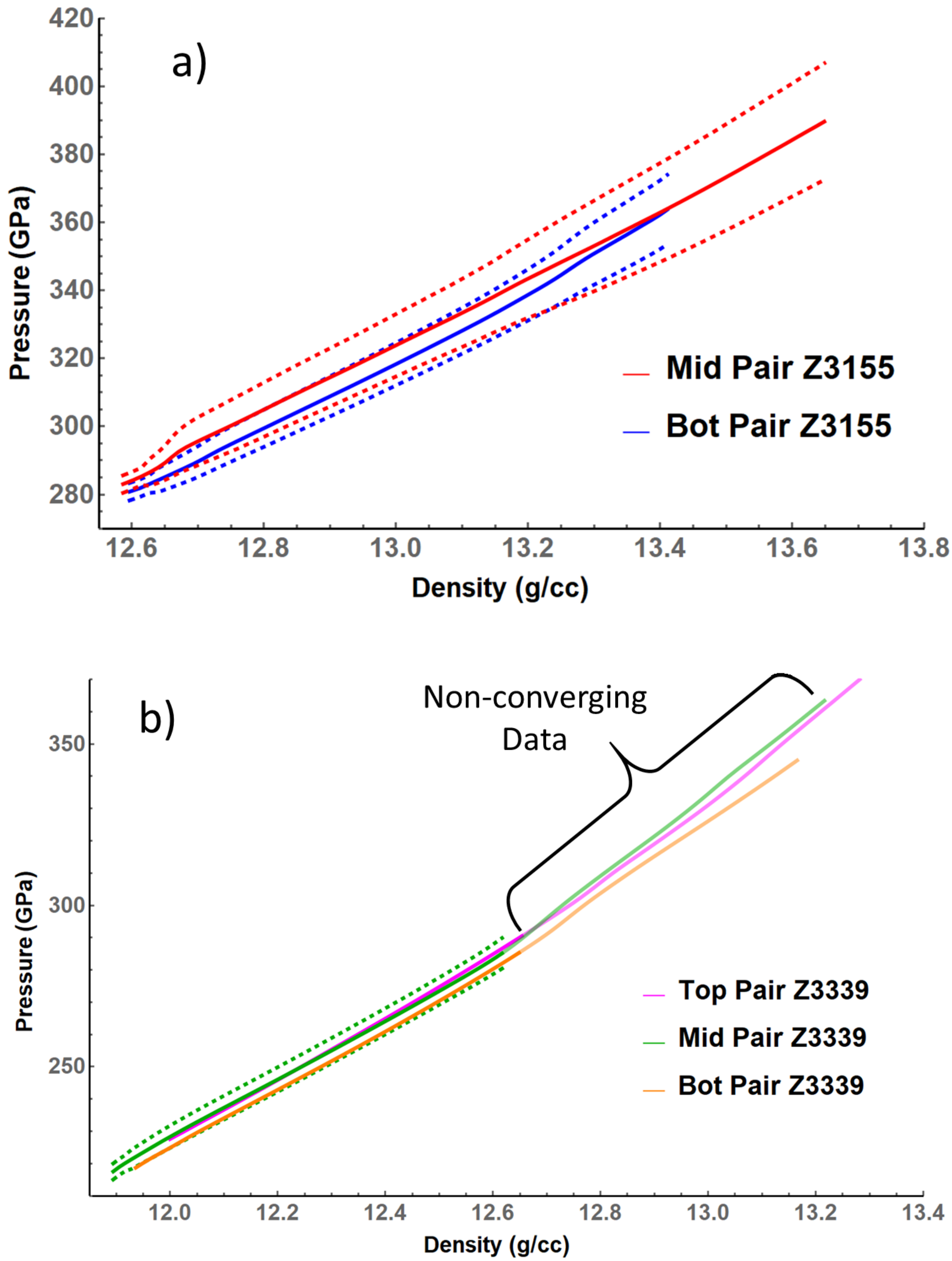

Figure 7. Pressure versus density profile of the iron sample pairs. **a)** shot Z3155 and **b)** shot Z3339. Error bounds of the profile are shown as dashed green lines. The error is only shown for

the middle pair on shot Z3339 for visual clarity. The data which does not converge in our iterative sound speed analysis is indicated and lightened.

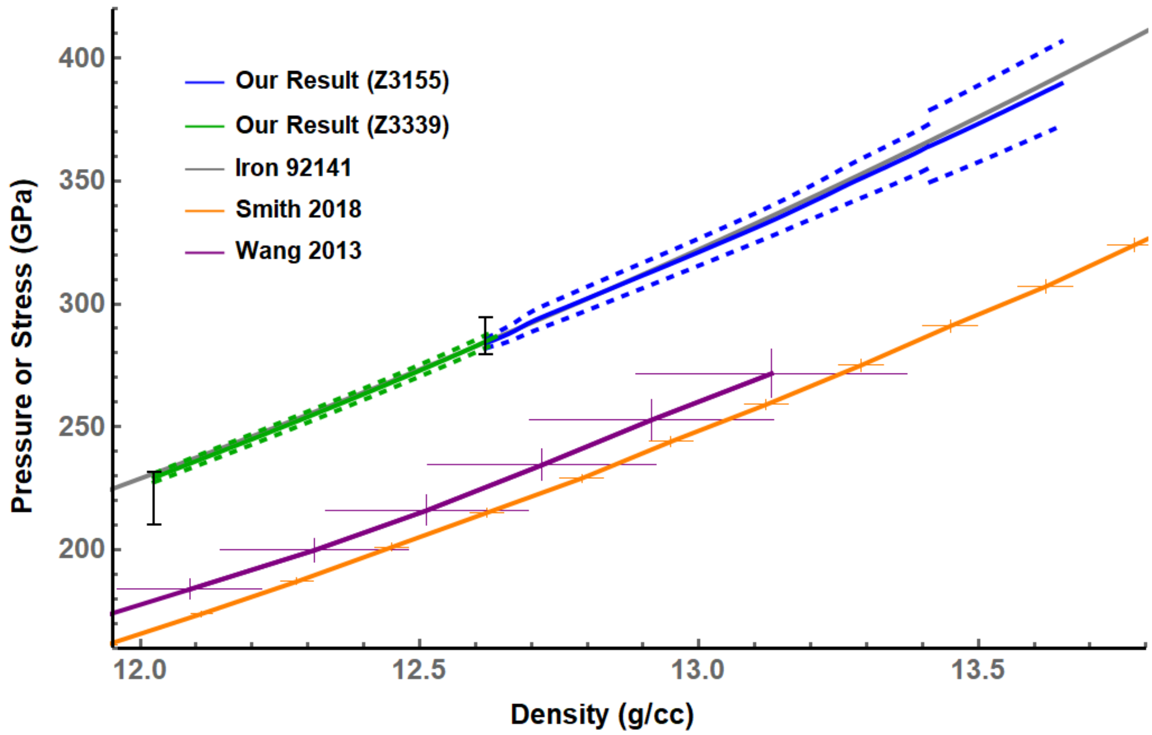

Figure 8. Pressure or stress versus density results. Our two elevated isentropes, shots Z3155 and Z3339 (blue and green, respectively), with error bounds shown as dashed lines, compared to the extracted profile from the iron SESAME 92141 EOS table (gray) (Sjostrom & Crockett, 2018) as well as the results from two solid off-Hugoniot ramp-compression experiments: stress-density results starting from 82 GPa (purple) (Wang et al., 2013) and reduced principal isentrope pressure-density results (orange) (Smith et al., 2018). Below 360 GPa, or 13.25 g/cc, the shot Z3155 trace is a combination of the two sample pairs, with error combined in quadrature, and above this point the trace is solely from the high-pressure sample pair.

For shot Z3339, the data analysis fails to converge beyond densities of 12.6 g/cc. We have confirmed that the modified analysis technique works on smoothly varying EOS traces via simulated experiments, so one possible explanation for this failure to converge is that the measured EOS is not smooth. The Hugoniot states in shot Z3339 are relatively low compared to our other experiments because of the shock wave decay that occurred in this experiment. This results in a smaller pressure difference between the Hugoniot and the melt line along the isentrope and makes shot Z3339 the most likely to have intersected the melt line via isentropic compression, and as we mentioned previously, sections of the sample may have even started ramp compression from a mixed-phase state. It is possible that this failure to converge resulted from phase-mixing interactions throughout the sample. The non-converging data are lightened and indicated in Figure 7b, but they were not included in the combined trace in Figure 8.

4 Results and implications

Our results cover the P-T range relevant to the ICB conditions and are applicable to building thermal EOS models for exoplanetary cores. Currently, the SESAME 92141 EOS covers the EOS of liquid iron at P-T conditions of the core, but has yet been applied to build planetary models. Our results are fully consistent with the SESAME 92141 EOS at the experimental P-T conditions of this study. For these reasons, we propose that our results as well as this table be used as the EOS for modeling iron planetary cores. Many previous planetary models implement their material EOS by using standardized EOS equations with experimentally or theoretically fitted parameters including Birch-Murnaghan EOS, Vinet EOS, and Mie-Gruneisen EOS (Cottaar et al., 2014; Seager et al., 2007; Unterborn et al., 2016; Valencia et al., 2006), but the input parameters were not experimentally verified at the realistic P-T conditions of those planetary interiors. Our EOS model covers the liquid iron data at realistic P-T conditions of Earth's ICB so it can be readily used to build an EOS model, in a vein similar to the work done already for the solid (Fei et al., 2016) to accommodate these modeling methods as well. We use both our off-Hugoniot isentrope data, as well as previous Hugoniot liquid data to complete this fit (Brown & McQueen, 1986). As mentioned previously, broad liquid EOS data are currently quite lacking. We include all of our valid data in this fitting process, treated as pressure data, as we are unable to distinguish any possible solid phase-mixing. In this section we also build radial planet models to analyze both mass-radius relations as well as the internal structure of planetary cores.

In the case of solid iron, there is already an extensive collection of data both overall in P-T conditions and at a known reference temperature (Fei et al., 2016). This allows the fitting to take place in two separate steps: fitting the parameters associated specifically with the isothermal reference state, and then those associated with the thermal contribution independently. Ideally, we would build our EOS in a similar manner, however, we do not have a similar collection of liquid data at a constant temperature. Therefore, we must fit all our parameters simultaneously, and even with the addition of the data presented here, we find that the many parameters involved in building the EOS are not adequately constrained. For this reason, we constrain some parameters from existing theoretical models to reduce the complexity of the fit. Several such theoretical works, which used different analytical forms for the EOS, already exist (Dorogokupets et al., 2017; Ichikawa et al., 2014; Komabayashi, 2014). We compare our data to three of these models and refine the model that matches the experimental data the best by fitting a few of the parameters to this experimental data.

In order to compare our data against these references and ultimately fit to an EOS model, we must assign temperature values to our pressure-density data. Since we do not measure the temperature of our samples in this experiment, we must estimate these values. For consistency, we assign the Hugoniot pinning points in our data a temperature such that it matches the same pressure condition in the shock Hugoniot data also being used within the fit (Brown & McQueen, 1986). Brown and McQueen (1986) did not explicitly account for the enthalpy of fusion in their Hugoniot data above the melt line, so we correct this in the referenced data. The entropy of fusion per atom calculated by Luo et al. (2011) is $0.83*k_b$. With the enthalpy of fusion being $H = S*T$, and an approximate melting temperature of 5500 K at 225 GPa, we estimate the enthalpy of fusion as 37.9 kJ/mol. Boness et al. (1986) calculated the approximate heat capacity in this region to be $4.4R$, including both vibrational and electronic terms. The temperature values given by Brown and McQueen (1986) are thus overestimated by H/C_V, or, given the uncertainties involved, approximately 1000 K. As for the rest of the elevated isentrope, we calculate the temperature using the γ parameter and the following equation for adiabatic temperature profiles:

$$dT = \frac{\gamma T}{V}\, dV \quad Eq. 13$$

where the γ used here is the effective Gruneisen parameter, $\gamma = -\left(\frac{\delta \ln T}{\delta \ln V}\right)_S$, which varies depending on the referenced form of the EOS. For each reference, self-consistent temperature values are calculated for our data by using the specific γ form and parameters contained within that reference.

We use the density and estimated temperature values from our data to calculate the pressure given by the model, and calculate the difference between this value and the value from our two data sets. These differences are plotted in Figure 9 which also include errors representing a combination of the error in our pressure data and the thermal pressure variance caused by a ±500 K temperature uncertainty. We have not included any error for the models in question as they do not all have error representations published. All three models encompass or almost encompass our data within uncertainties. To choose which model fits our data the best, we calculate the square sum of these differences, and choose the set with the smallest value. The model using Ichikawa et al. (2014) as a reference fits the best, so we build our analytical EOS via refitting some parameters of the Ichikawa model.

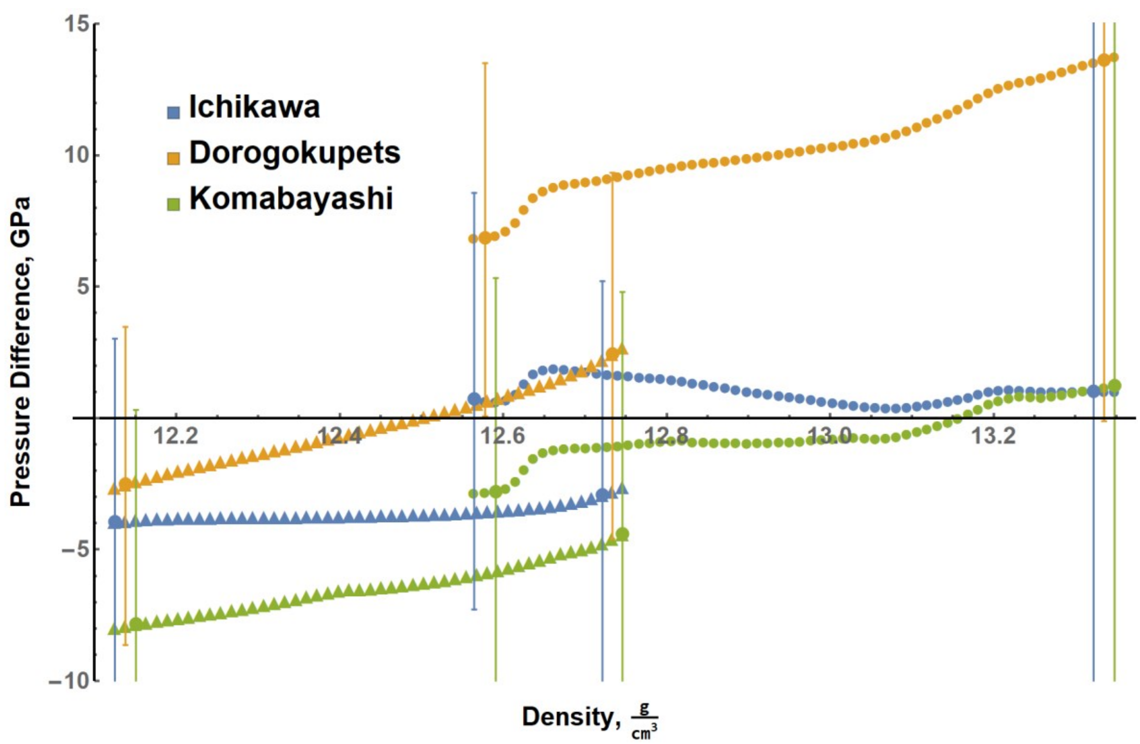

Figure 9. Pressure difference between our data sets, shot Z3155 (circles) and shot Z3339 (triangles), and reference models. Reference models include Ichikawa et al. (2014) (Blue), Komabayashi (2014) (Green), and Dorogokupets et al. (2017) (Orange). Representative error for each set is shown near the endpoints; this error represents a combination of the pressure error in

our data and a modeled thermal pressure uncertainty resulting from a ±500 K temperature uncertainty.

We fit our data using the same model Ichikawa et al. (2014) used so that we can implement similar parameters from their model, as necessary, to further constrain our fitting parameters. We note that Ichikawa et al. (2014) used a Vinet-Rydberg (Vinet et al., 1989) formulation for the isothermal part of their EOS:

$$P_{iso}(\rho) = 3\,K_0\left(\frac{\rho}{\rho_0}\right)^{\frac{2}{3}}\left(1-\left(\frac{\rho_0}{\rho}\right)^{\frac{1}{3}}\right)Exp\left[\frac{3}{2}(K_0'-1)\left(1-\left(\frac{\rho_0}{\rho}\right)^{\frac{1}{3}}\right)\right] \quad Eq. 14$$

where *P* is pressure, *K* is the bulk modulus, *K'* is the pressure derivative of the bulk modulus, and ρ is the density; a 0 subscript represents these values at the reference state of 7000 K and 0 GPa pressure. The thermal component of their EOS is considered using a thermal energy term of the form:

$$E_{th}(\rho,T) = 3nR\left[T + e_0\left(\frac{\rho_0}{\rho}\right)^g T^2\right] \quad Eq. 15$$

where *T* is temperature, *n* is the number of atoms in the formula unit, *R* is the gas constant, and e_0 is the electronic parameter, and *g* is the electronic analogue to the Gruneisen parameter. The first term represents the phonon energy contribution while the second represents the electronic contribution. The thermal pressure contribution to the EOS, formulated with the Gruneisen parameter, γ, is:

$$P_{th}(\rho,T) = \gamma(\rho)\,\rho\,(E_{th}(\rho,T) - E_{th}(\rho,T_0)) \quad Eq. 16$$

and they adopt the functional form of γ from Tange et al. (2009):

$$\gamma(\rho) = \gamma_0\left[1 + a\left(\left(\frac{\rho_0}{\rho}\right)^b - 1\right)\right] \quad Eq. 17$$

where *a* and *b* are both fitted parameters.

As our isentropic data traces cover broader ranges of pressure and density than temperature, we have chosen to keep K_0 and K_0' as two of our fitting parameters since they relate strongly to these two state variables. We found that the fitting could handle three parameters well, so we have also included γ_0 as a fitting parameter. The other parameters are all taken from Ichikawa et al. (2014). We incorporate the ± 500 K temperature uncertainty into this fitting procedure by repeating the fit three times, once with our initially assumed temperature, and then the whole process repeated twice, once with the temperature value increased by 500 K and once decreased by 500 K. We take the average of these three results and increase the error by the difference from the extremes. We consider this an accurate implementation of the error as this temperature error is systematic. The results of the fitting are shown in Table 2.

Parameter	**Ichikawa values**	**Fit values**
K_0 (GPa)	24.6 ± 0.6	25.3 ± 4.0
K_0'	6.65 ± 0.04	6.60 ± 0.33
ρ_0 (g/cc)	5.187	

γ_0	1.85 ± 0.2	2.42 ± 0.12
a	1	
b	0.35	
e_0 (10^{-4}/K)	0.314	
g	-0.4	

Table 2. Fitting parameters for the liquid EOS of iron. The values from Ichikawa et al. are shown in the first column (Ichikawa et al., 2014), while the second column shows the values we obtained from our fit. The reference parameters are taken at 7000 K and 0 GPa.

As mentioned previously, the calculated temperature values we estimated for our data depend on γ, but γ depends on the fit parameter, γ_0. In order to maintain the internal consistency, after the first fit is done, using temperature values based on the value of γ_0 in the reference, we recalculate the temperature values based on the new fit. We perform the fit again with the new temperature values and iterate the processes until the derived fit parameters are consistent with those used to generate the temperature values for our data. In Figure 10, we compare this fit to our experimental data for iron.

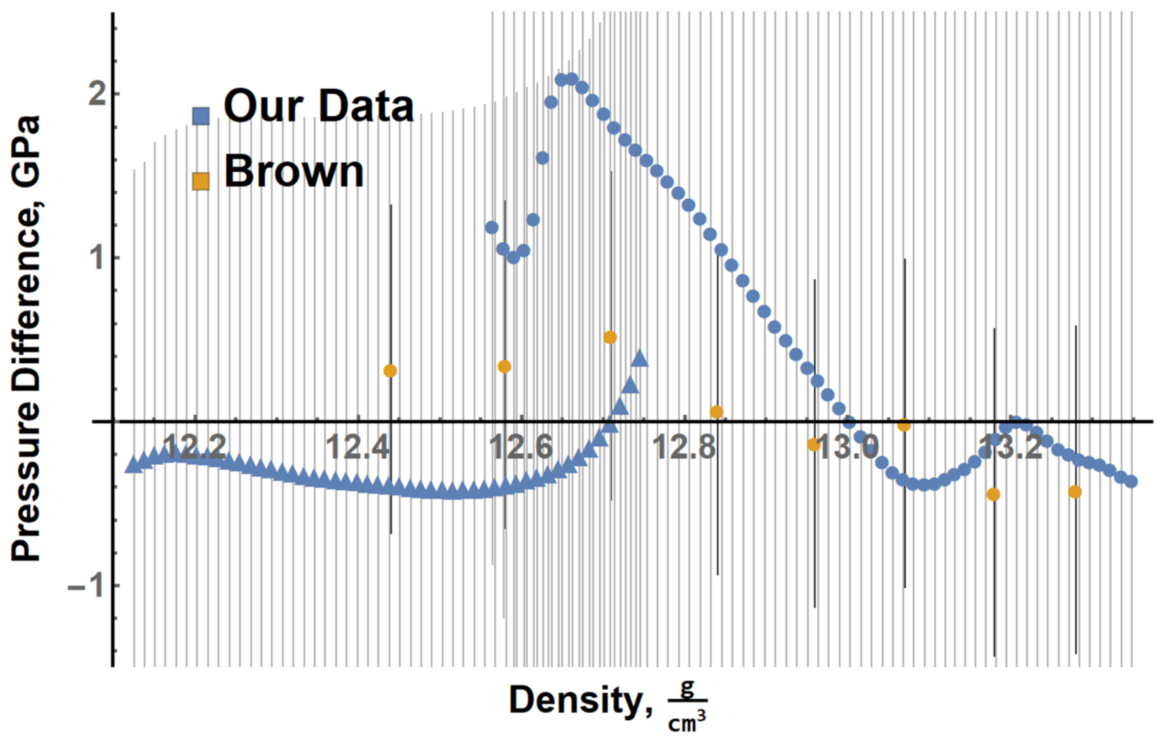

Figure 10. Pressure difference between the fit EOS and the data as a function of density. The data are from Brown and McQueen (1986) (orange circles) and our work, Z3155 (blue circles) and Z3339 (blue triangles).

We have presented two methods to simulate the behavior of liquid iron – an experimentally validated EOS table and a parametrized analytic EOS. Most planetary models treat the whole of the core as a solid, but with these two options, the inclusion of separate liquid and solid layers in the core can be incorporated into these models to improve accuracy – either explicitly using the analytic EOS, or implicitly through the multiphase SESAME EOS table. We present an example of this by building radial models of example planets.

The techniques we present and use here to build these radial models have a rich history in literature (Fortney et al., 2007; Grasset et al., 2009; Guillot et al., 1996; Seager et al., 2007; Stevenson, 1982; Swift et al., 2012; Unterborn et al. 2016; Unterborn & Panero, 2019; Valencia et al., 2006; Wagner et al., 2011; Zapolsky & Salpeter, 1969; Zeng et al., 2016). We implement the multiphase iron SESAME 92141 EOS, that is supported by our new data and previously unused for this type of application, into this existing framework. These models start with the Adam-Williamson Equations (Williamson & Adams, 1923) – equations for pressure, density, and mass as a function of radius for a spherically symmetric system under equilibrium and gravitational compression– as well as the equation for an adiabatic temperature profile:

$$\frac{dm}{dr} = 4\pi r^2 \rho \quad Eq. 18$$

$$\frac{dP}{dr} = -\frac{\rho\, G\, m(r)}{r^2} \quad Eq. 19$$

$$\rho(r) = \rho_{eos}(P(r), T) \quad Eq. 20$$

$$\frac{dT}{dr} = -\frac{\alpha\big(T(r)\big)\frac{Gm(r)}{r^2}T(r)}{C_P} \quad Eq. 21$$

m, P, ρ, and T are mass, pressure, density and temperature, respectively, as a function of radius, r. C_P, α, and G are the isobaric heat capacity, thermal expansion coefficient, and gravitational constant, respectively. ρ_{eos} is the ρ to P relation based on the EOS being used to represent the material within the planet, which could either be an analytical form of the EOS or extractions from a tabular EOS. This provides a series of differential equations that can be solved with appropriate boundary conditions. The temperature equation assumes an adiabatic temperature profile with radius because of vigorous convections of the liquid iron core, as is expected for planets with dynamos and magnetic fields that would have a good chance of supporting life (Langmuir and Broecker, 2012). When using an EOS table, this adiabatic temperature-radius profile is established by constraining the EOS function to an isentropic curve extracted from the table – eliminating the need for the temperature equation, Equation 21. There are multiple ways to proceed with these boundary conditions, we start with a defined core temperature and density, and integrate radially outwards from r=0. For a planet made of a single material, the calculation is complete once the pressure reaches zero, defining the outer radius of the planet, $P(R) = 0$.

As a preliminary analysis, we create a simple planetary model of a homogeneous, isothermal, pure iron planet at 300 K using the SESAME 92141 table for the EOS. As this is an isothermal model, an isotherm is extracted from the SESAME EOS instead of an isentrope. One particularly useful metric, given the values returned from planetary search programs, is the mass-radius relation of planets. With this we can estimate the composition of observed planets based on their reported mass and radius. We generate such a curve by running the planetary model over a range of inner core pressures, generating planets of varying size and mass. Figure 11 shows the mass-radius curve generated for this model in comparison to that of the homogeneous, 300 K, pure-iron planets from Seager et al. (2007). Seager et al. use an EOS that is a combination of a Vinet for pressures up to 2090 GPa (Anderson et al., 2001) and a modified Thomas-Fermi-Dirac model for higher pressures (Salpeter and Zapolsky, 1967). Our curve agrees well with the referenced results. This provides a quick check that our modeling technique and the SESAME values at low temperatures are reliable.

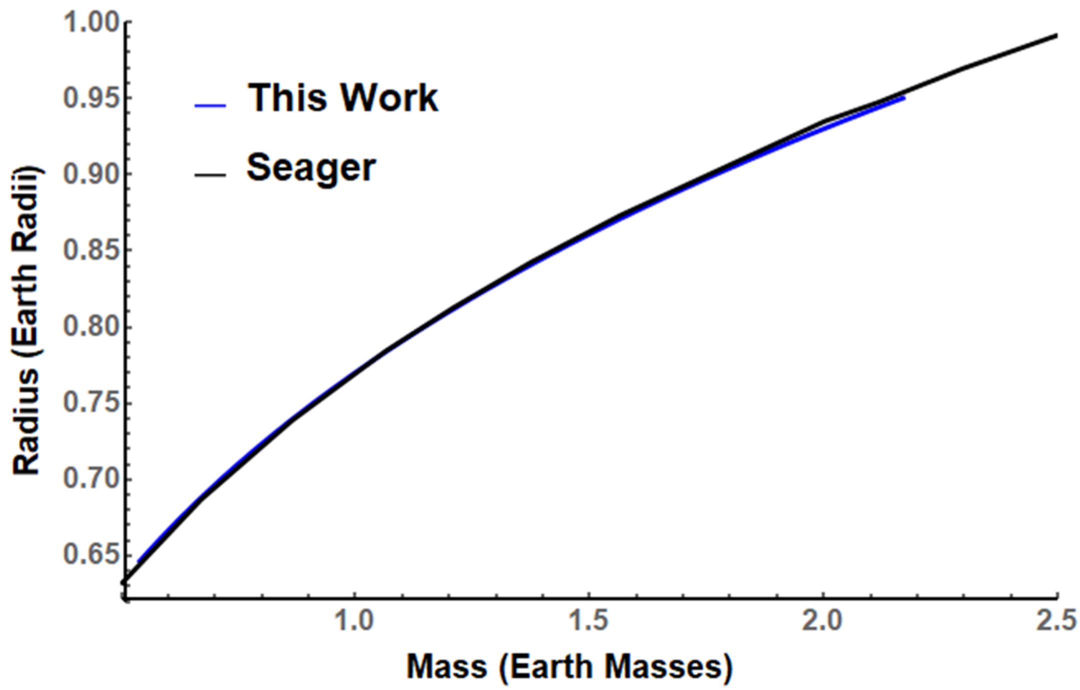

Figure 11. Mass-radius curve of homogeneous, isothermal, pure iron planets at 300 K temperature. This work (blue) using the SESAME 92141 table, in comparison to the results of Seager et al. (2007) (black).

Most planets are neither isothermal nor made of a single material, so we also build planetary models with multiple layers of different materials each constrained to an adiabat. The interface boundary is handled simply by imposing that at any given interface, the two layers have equal pressure and an imposed temperature jump, but we must decide how to dictate the location of the layer boundaries. In principle, the easiest method is to dictate a radius at which the interface occurs. However, this is not particularly useful, especially when the outer radius of the planet is unknown. It is more useful to model planets that have specific mass or radius ratios between the layers. For instance, Earth has a core mass fraction of ~32%, so we may want to see how well our model builds a similar planet to Earth or a planet with a similar core mass fraction of different total sizes. We have opted to pursue this route, where the mass fraction of the core layer is defined.

As an example, take a two-layer planet, with an iron core and $MgSiO_3$ perovskite mantle. The final mass of the planet, M, is still unknown while the integration is being run, so we cannot know exactly where to set the boundary layer location, r_b, a priori. To handle this, we use an iterative process. We start with a guess for the total mass of the planet, M_{guess}, and designate the layer interface to occur where the mass of the inner layer reaches the desired mass fraction of the assumed total mass, $m(r_b) = 0.32*M_{guess}$, where we have chosen an Earth-like core mass fraction. The integration continues into the mantle layer, and the calculation completes when the pressure reaches zero, defining the outer radius of the planet. With a completed planet, the actual total mass is known, and the mass fraction evaluated. If the core mass fraction is not sufficiently close to the desired value, we chose 32 ± 0.2%, then the whole process can be repeated with the new total mass replacing the initial guess. Repeating this process causes the layer boundary location to converge upon the appropriate value for a given core mass fraction.

In our models, the mantle EOS uses the parameters presented by Katsura (Katsura et al., 2010), based on a Birch-Murnaghan isothermal EOS (Birch, 1952) with a Mie-Gruneisen-Debye thermal model (Grüneisen, 1912), and the iron core uses an extracted isentrope from the SESAME 92141 EOS table. The isentrope extracted from the table has a 2000 K ambient pressure intercept. One benefit of the multi-phase SESAME 92141 EOS table is that it inherently accounts for any phase change. Our chosen isentrope intersects the melt line at 400 GPa; this gives a P-T curve that runs close to the melt line, allowing a solid inner core to form, as well as the presence of an active core dynamo in a liquid layer powered by thermal cooling, latent heat, as well as release of light elements. As both the isentrope and the melt line are relatively flat in temperature, the presence and location of the inner core boundary is relatively sensitive to changes in temperature. Therefore, we note that these results represent a snapshot in the cooling-history of these modeled planets. We impose a 1000 K temperature drop across the core-mantle boundary as a reasonable approximation for near-Earth-size planets. We present the pressure, density, and temperature curves for a 1.2 Earth mass planet in Figure 12.

Figure 13 shows our mass-radius curve for an Earth-like planet compared with previous literature (Seager et al., 2007). The mantle EOS used in Seager et al. (2007) is a fourth-order Birch-Murnaghan EOS (Karki et al., 2000) for pressures up to 1350 GPa and a modified Thomas-Fermi-Dirac model at higher pressures (Salpeter and Zapolsky, 1967), and they use a 300 K isothermal planetary model. Mass-radius curves from a range of planetary compositions can help identify the possible composition of observed extraterrestrial planets. For instance, an observed planet with a mass and radius that locates the planet between our two curves would likely indicate that the planet is rocky with a larger core mass fraction than the Earth. Our curve is in close agreement with that of Seager et al. (2007), however we note that this does not mean these changes have no effect overall. In the formulation used here, where planets are built with a certain core-mass ratio, the mass-radius curve is insensitive to density scaling of the core material, despite the central density and core size being noticeably different for a given planetary mass – Grasset et al. (2009) come to similar conclusions in their work. With this constant isentrope being used for the core, we find that a liquid outer core is only present in planets below 3.1 Earth masses, but this result is sensitive to the temperature of the planet. At early formations of exoplanetary interiors, their core temperatures are likely much higher than the melting curve of iron so solid inner cores could not solidify and silicate mantles could be molten or partially molten. It is when these planets cool to the point that intersects the iron melting curve at somewhere around 6000-8000 K depending on their masses (Fig. 1), that the solidification of iron in these planets would have chemical energy and latent heat energy sources, in addition to the thermal cooling energy, to power their core convections and dynamos. Importantly, those planets would have a chance to develop solid mantles to allow stable convections and heat transports similar to Earth's plate tectonics system and mantle convections. For example, if we instead use an isentrope with a 3000 K zero pressure intercept, we find that the mass-radius curve is minimally affected, but the cores of these planets do not begin to solidify until approximately 3 Earth masses. This means that planets between 1 and 3 Earth masses would all contain a growing solid inner core at some point as they cool between these two temperature conditions. We also modeled planets using a 4000 K ambient pressure intercept for the iron isentrope, where the high temperature keeps the iron cores molten well beyond the planetary masses we calculated. The effect of this temperature increase on the mass-radius relation can be seen in Figure 13. Note that while the temperature difference between the two presented isentropes is 2000 K at ambient pressure, this difference increases with pressure and is close to 4000 K in the region near the melt line. This highlights that while mass-radius curves are becoming relatively well defined, there are still many uncertainties that apply to important internal structure – such as the presence and location of a liquid-solid boundary in the core. We should note that future studies on the EOS and melting curves of iron-light element alloys at extreme P-T conditions are critically needed to better evaluate physical and chemical evolutions of exoplanetary interiors.

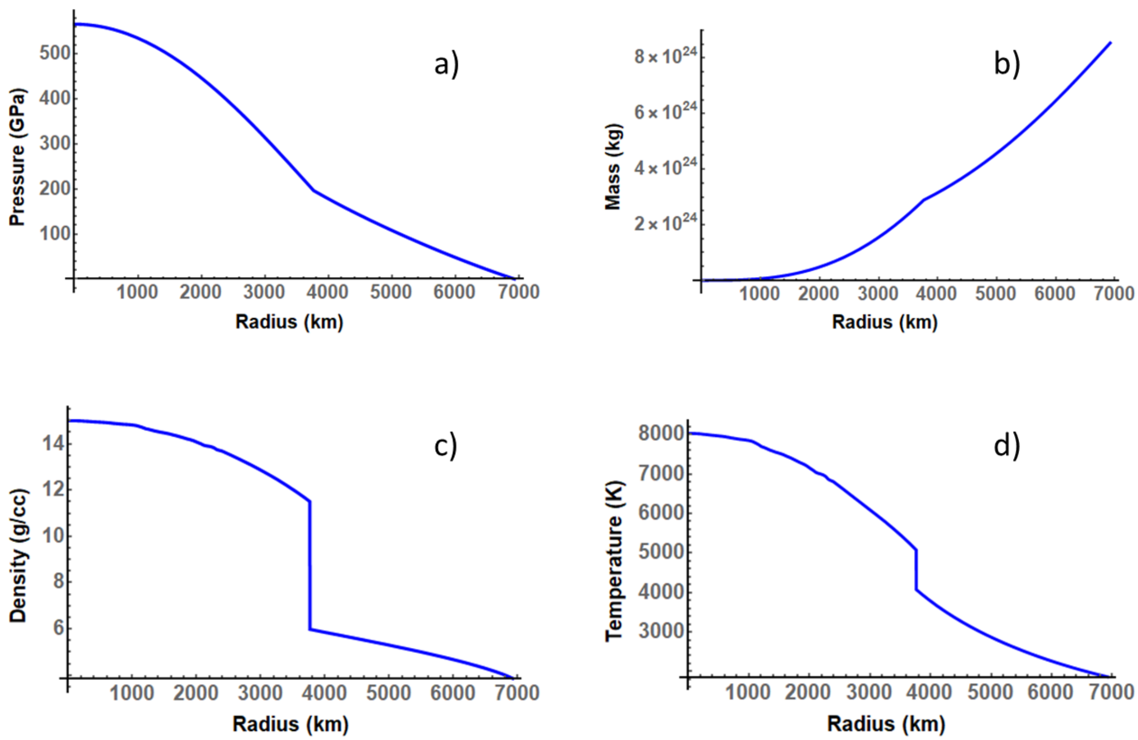

Figure 12. a) Pressure, **b)** mass, **c)** density, and **d)** temperature as a function of radius for a 1.2 Earth mass planet with an Earth-like core mass ratio. Generated using the iron isentrope with a 2000 K ambient pressure intercept.

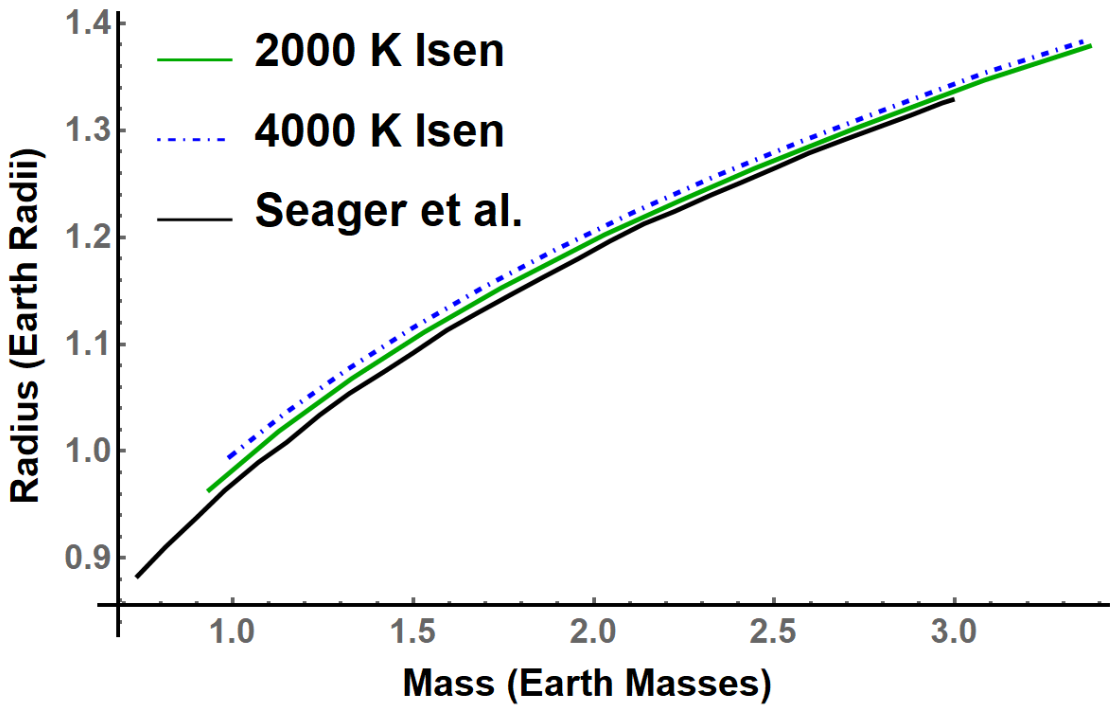

Figure 13. Mass-radius curve of planets with an Earth-like core mass ratio. This work, 2000 K ambient pressure intercept (green) and 4000 K ambient pressure intercept (blue dashed), using the SESAME 92141 table for the core, in comparison to the 300 K isothermal results of Seager et al. (2007) (black).

This work, and many current planetary models, treat the cores as pure iron. However, the cores of planets are made of iron alloys (Birch, 1952). Some planetary modelling has attempted to account for this by scaling the density of a pure iron EOS (Unterborn et al., 2016), which is a reasonable assumption given our current knowledge, but it would be extremely useful to have experimental results on these materials. These in turn will also help us evaluate the magnitude of the chemical energy source for the generation of planetary dynamos. We are extending these experiments to iron alloys as well, with the hope of granting insight into the accuracy and implications of these current assumptions.

5 Conclusions

We performed shock-ramp experiments on the Z-Machine at Sandia National Laboratories to measure the EOS of liquid or near-liquid iron along an elevated ramp compression path by pushing the limits of what is currently capable on this machine. We initially shock the iron to 270 GPa, melting the iron sample; the samples undergo a combination of growing or decaying shock, and ramp compression or release before ultimately being ramp compressed by 100 GPa or more. The iterative backward integration – forward Lagrangian analysis is used to determine the pressure-density EOS along this ramp path. Our results show excellent agreement with the SESAME 92141 EOS table for iron at the P-T conditions covered by this study. Further, we apply these results to the study of planetary structures via radial models. We find that the mass-radius curve of planets with an Earth-like core mass ratio is insensitive to density change in the core as well as temperature, and that our results are in good agreement with existing literature. By implementing a multi-phase iron EOS, we are able to investigate the presence of a liquid-solid phase boundary within the core and we note the maximum and/or minimum planet masses of planets which contain an ICB for several temperature adiabats.

Acknowledgments, Samples, and Data

Data supporting this research are available upon request to S.G., after Sandia National Laboratories review and approval for release.

The authors thank the Z-Machine operations, engineering, and diagnostics staff for their critical role in the performance of these experiments, and the support and advocacy of Dawn Flicker and John Benage. We also acknowledge generous financial support by Sandia National Laboratories. S.G. would like to thank SEERI and the Student Intern Program at Sandia National Laboratories for their support. Experimental time on the Z facility was provided through the Z Fundamental Science Program. The authors also thank the anonymous reviewers for their helpful comments.

This paper describes objective technical results and analysis. Any subjective views or opinions that might be expressed in the paper do not necessarily represent the views of the U.S. Department of Energy or the United States Government.

Sandia National Laboratories is a multimission laboratory managed and operated by National Technology & Engineering Solutions of Sandia, LLC, a wholly owned subsidiary of Honeywell International Inc., for the U.S. Department of Energy's National Nuclear Security Administration under contract DE-NA0003525.

References

Alfè, D., Price, G. D., & Gillan, M. J. (2002). Iron under Earth's core conditions: Liquid-state thermodynamics and high-pressure melting curve from ab initio calculations. *Physical Review B*, *65*(16), 165118.

Anderson, O. L., Dubrovinsky, L., Saxena, S. K., & LeBihan, T. (2001). Experimental vibrational Grüneisen ratio values for ϵ-iron up to 330 GPa at 300 K. *Geophysical research letters*, *28*(2), 399-402.

Anzellini, S., Dewaele, A., Mezouar, M., Loubeyre, P., & Morard, G. (2013). Melting of iron at Earth's inner core boundary based on fast X-ray diffraction. *Science*, *340*(6131), 464-466.

Ao, T., Knudson, M. D., Asay, J. R., & Davis, J.-P. (2009). Strength of lithium fluoride under shockless compression to 114 GPa. *Journal of Applied Physics*, *106*(10), 103507. Barker, L. M., & Hollenbach, R. E. (1972). Laser interferometer for measuring high velocities of any reflecting surface. *Journal of Applied Physics*, *43*(11), 4669-4675.

Bastea, M., Bastea, S., & Becker, R. (2009). High pressure phase transformation in iron under fast compression. *Applied Physics Letters*, *95*(24), 241911.

Batalha, N. M., Borucki, W. J., Bryson, S. T., Buchhave, L. A., Caldwell, D. A., Christensen-Dalsgaard, J., Ciardi, D., Dunham, E. W., Fressin, F., Gautier III, T. N. & Gilliland, R. L. (2011). Kepler's first rocky planet: Kepler-10b. *The Astrophysical Journal*, *729*(1), 27.

Birch, F. (1952). Elasticity and constitution of the Earth's interior. *Journal of Geophysical Research*, *57*(2), 227-286.

Boness, D. A., Brown, J. M., & McMahan, A. K. (1986). The electronic thermodynamics of iron under Earth core conditions. *Physics of the Earth and Planetary Interiors*, *42*(4), 227-240.

Brown, J. M., & McQueen, R. G. (1986). Phase transitions, Grüneisen parameter, and elasticity for shocked iron between 77 GPa and 400 GPa. *Journal of Geophysical Research: Solid Earth*, *91*(B7), 7485-7494.

Buffett, B. A. (2000). Earth's core and the geodynamo. *Science*, *288*(5473), 2007-2012.

Busse, F. H. (1976). Generation of planetary magnetism by convection. *Physics of the Earth and Planetary Interiors*, *12*(4), 350-358.

Chen, G. Q., & Ahrens, T. J. (1997). High pressure and high temperature equation-of-state of gamma and liquid iron. *MRS Online Proceedings Library Archive*, *499*.

Cottaar, S., Heister, T., Rose, I., & Unterborn, C. (2014). BurnMan: A lower mantle mineral physics toolkit. *Geochemistry, Geophysics, Geosystems*, *15*(4), 1164-1179.

Davis, J. P. (2006). Experimental measurement of the principal isentrope for aluminum 6061-T6 to 240 GPa. *Journal of applied physics*, *99*(10), 103512.

Davis, J. P., Knudson, M. D., Shulenburger, L., & Crockett, S. D. (2016). Mechanical and optical response of [100] lithium fluoride to multi-megabar dynamic pressures. *Journal of Applied Physics*, *120*(16), 165901.

Dewaele, A., Loubeyre, P., Occelli, F., Mezouar, M., Dorogokupets, P. I., & Torrent, M. (2006). Quasihydrostatic equation of state of iron above 2 Mbar. *Physical Review Letters*, *97*(21), 215504.

Dolan, D. H. (2006). *Foundations of VISAR analysis* (No. SAND2006-1950). Sandia National Laboratories.

Dorogokupets, P. I., Dymshits, A. M., Litasov, K. D., & Sokolova, T. S. (2017). Thermodynamics and Equations of State of Iron to 350 GPa and 6000 K. *Scientific reports*, *7*(1), 1-11.

Fei, Y., Murphy, C., Shibazaki, Y., Shahar, A., & Huang, H. (2016). Thermal equation of state of hcp-iron: Constraint on the density deficit of Earth's solid inner core. *Geophysical Research Letters*, *43*(13), 6837-6843.

Fortney, J. J., Marley, M. S., & Barnes, J. W. (2007). Planetary radii across five orders of magnitude in mass and stellar insolation: application to transits. *The Astrophysical Journal*, *659*(2), 1661.

Gillon, M., Triaud, A. H., Demory, B. O., Jehin, E., Agol, E., Deck, K. M., Lederer, S. M., De Wit, J., Burdanov, A., Ingalls, J. G. & Bolmont, E. (2017). Seven temperate terrestrial planets around the nearby ultracool dwarf star TRAPPIST-1. *Nature*, *542*(7642), 456-460.

Grasset, O., Schneider, J., & Sotin, C. (2009). A study of the accuracy of mass-radius relationships for silicate-rich and ice-rich planets up to 100 Earth masses. *The Astrophysical Journal*, *693*(1), 722.

Grüneisen, E. (1912). Theorie des festen Zustandes einatomiger Elemente. *Annalen der Physik*, *344*(12), 257-306.

Guillot, T., Burrows, A., Hubbard, W. B., Lunine, J. I., & Saumon, D. (1996). Giant planets at small orbital distances. *The Astrophysical Journal Letters*, *459*(1), L35.

Hall, C. A., Asay, J. R., Knudson, M. D., Stygar, W. A., Spielman, R. B., Pointon, T. D., Reisman, D. B., Toor, A. & Cauble, R. C. (2001). Experimental configuration for isentropic compression of solids using pulsed magnetic loading. *Review of Scientific Instruments*, *72*(9), 3587-3595.

Hayes, D. B. (2001). *Backward integration of the equations of motion to correct for free surface perturbations* (No. SAND2001-1440). Sandia National Labs., Albuquerque, NM (US); Sandia National Labs., Livermore, CA (US).

Ichikawa, H., Tsuchiya, T., & Tange, Y. (2014). The P-V-T equation of state and thermodynamic properties of liquid iron. *Journal of Geophysical Research: Solid Earth*, *119*(1), 240-252.

Karki, B. B., Wentzcovitch, R. M., De Gironcoli, S., & Baroni, S. (2000). Ab initio lattice dynamics of MgSiO 3 perovskite at high pressure. *Physical Review B*, *62*(22), 14750.

Katsura, T., Yoneda, A., Yamazaki, D., Yoshino, T., & Ito, E. (2010). Adiabatic temperature profile in the mantle. *Physics of the Earth and Planetary Interiors*, *183*(1-2), 212-218.

Kerley, G. I. (1987). Theoretical equation of state for aluminum. *International Journal of Impact Engineering*, *5*(1-4), 441-449.

Komabayashi, T. (2014). Thermodynamics of melting relations in the system Fe-FeO at high pressure: Implications for oxygen in the Earth's core. *Journal of Geophysical Research: Solid Earth*, *119*(5), 4164-4177.

Konôpková, Z., McWilliams, R. S., Gómez-Pérez, N., & Goncharov, A. F. (2016). Direct measurement of thermal conductivity in solid iron at planetary core conditions. *Nature*, *534*(7605), 99-101.

Langmuir, C. H., & Broecker, W. (2012). *How to Build a Habitable Planet: The Story of Earth from the Big Bang to Humankind-Revised and Expanded Edition*. Princeton University Press.

Léger, A., Grasset, O., Fegley, B., Codron, F., Albarede, A. F., Barge, P., Barnes, R., Cance, P., Carpy, S., Catalano, F. & Cavarroc, C. (2011). The extreme physical properties of the CoRoT-7b super-Earth. *Icarus*, *213*(1), 1-11.

Léger, A., Rouan, D., Schneider, J., Barge, P., Fridlund, M., Samuel, B., Ollivier, M., Guenther, E., Deleuil, M., Deeg, H. J. & Auvergne, M. (2009). Transiting exoplanets from the CoRoT space mission-VIII. CoRoT-7b: the first super-Earth with measured radius. *Astronomy & Astrophysics*, *506*(1), 287-302.

Lemke, R. W., Knudson, M. D., Bliss, D. E., Cochrane, K., Davis, J. P., Giunta, A. A., Harjes, H. C. & Slutz, S. A. (2005). Magnetically accelerated, ultrahigh velocity flyer plates for shock wave experiments. *Journal of Applied Physics*, *98*(7), 073530.

Lemke, R. W., Knudson, M. D., & Davis, J. P. (2011). Magnetically driven hyper-velocity launch capability at the Sandia Z accelerator. *International Journal of Impact Engineering*, *38*(6), 480-485.

Li, J., Wu, Q., Li, J., Xue, T., Tan, Y., Zhou, X., Zhang, Y., Xiong, Z., Gao, Z. and Sekine, T. (2020). Shock melting curve of iron: A consensus on the temperature at the Earth's inner core boundary. *Geophysical Research Letters*, *47*(15), e2020GL087758.

Luo, F., Cheng, Y., Chen, X. R., Cai, L. C., & Jing, F. Q. (2011). The melting curves and entropy of iron under high pressure. *Journal of Chemical & Engineering Data*, *56*(5), 2063-2070.

Marcy, G. W., Isaacson, H., Howard, A. W., Rowe, J. F., Jenkins, J. M., Bryson, S. T., Latham, D. W., Howell, S. B., Gautier III, T. N., Batalha, N. M. & Rogers, L. (2014). Masses, radii, and orbits of small Kepler planets: the transition from gaseous to rocky planets. *The Astrophysical Journal Supplement Series*, *210*(2), 20.

Maw, J. R. (2004, July). A characteristics code for analysis of isentropic compression experiments. In *AIP Conference Proceedings* (Vol. 706, No. 1, pp. 1217-1220). American Institute of Physics.

Morard, G., Andrault, D., Antonangeli, D., & Bouchet, J. (2014). Properties of iron alloys under the Earth's core conditions. *Comptes Rendus Geoscience*, *346*(5-6), 130-139.

Morard, G., Boccato, S., Rosa, A. D., Anzellini, S., Miozzi, F., Henry, L., Garbarino, G., Mezouar, M., Harmand, M., Guyot, F. & Boulard, E. (2018). Solving controversies on the iron phase diagram under high pressure. *Geophysical Research Letters*, *45*(20), 11-074.

Morard, G., Siebert, J., Andrault, D., Guignot, N., Garbarino, G., Guyot, F., & Antonangeli, D. (2013). The Earth's core composition from high pressure density measurements of liquid iron alloys. *Earth and Planetary Science Letters*, *373*, 169-178.

Murphy, C. A., Jackson, J. M., Sturhahn, W., & Chen, B. (2011). Melting and thermal pressure of hcp-Fe from the phonon density of states. *Physics of the Earth and Planetary Interiors*, *188*(1-2), 114-120.

Nguyen, J. H., & Holmes, N. C. (2004). Melting of iron at the physical conditions of the Earth's core. *Nature*, *427*(6972), 339-342.

Ohta, K., Kuwayama, Y., Hirose, K., Shimizu, K., & Ohishi, Y. (2016). Experimental determination of the electrical resistivity of iron at Earth’s core conditions. *Nature*, *534*(7605), 95-98.

Ping, Y., Coppari, F., Hicks, D. G., Yaakobi, B., Fratanduono, D. E., Hamel, S., Eggert, J. H., Rygg, J. R., Smith, R. F., Swift, D. C. & Braun, D. G. (2013). Solid iron compressed up to 560 GPa. *Physical review letters*, *111*(6), 065501.

Porwitzky, A., Hutsel, B. T., Seagle, C. T., Ao, T., Grant, S., Bernstein, A., Lin, J. F. & Ditmire, T. (2019). Large time-varying inductance load for studying power flow on the Z machine. *Physical Review Accelerators and Beams*, *22*(9), 090401.

Ricker, G. R., Winn, J. N., Vanderspek, R., Latham, D. W., Bakos, G. Á., Bean, J. L., Berta-Thompson, Z. K., Brown, T. M., Buchhave, L., Butler, N. R. & Butler, R. P. (2014). Transiting exoplanet survey satellite. *Journal of Astronomical Telescopes, Instruments, and Systems*, *1*(1), 014003.

Rigg, P. A., Knudson, M. D., Scharff, R. J., & Hixson, R. S. (2014). Determining the refractive index of shocked [100] lithium fluoride to the limit of transmissibility. *Journal of Applied Physics*, *116*(3), 033515.

Rogers, L. A., & Seager, S. (2010). A framework for quantifying the degeneracies of exoplanet interior compositions. *The Astrophysical Journal*, *712*(2), 974.

Rothman, S. D., Davis, J. P., Maw, J., Robinson, C. M., Parker, K., & Palmer, J. (2005). Measurement of the principal isentropes of lead and lead–antimony alloy to∼ 400 kbar by quasi-isentropic compression. *Journal of Physics D: Applied Physics*, *38*(5), 733.

Rothman, S. D., & Maw, J. (2006, August). Characteristics analysis of isentropic compression experiments (ICE). In *Journal de Physique IV (Proceedings)* (Vol. 134, pp. 745-750). EDP sciences.

Salpeter, E. E., & Zapolsky, H. S. (1967). Theoretical high-pressure equations of state including correlation energy. *Physical Review*, *158*(3), 876.

Sanloup, C., Van Westrenen, W., Dasgupta, R., Maynard-Casely, H., & Perrillat, J. P. (2011). Compressibility change in iron-rich melt and implications for core formation models. *Earth and Planetary Science Letters*, *306*(1-2), 118-122.

Savage, M. E., Bennett, L. F., Bliss, D. E., Clark, W. T., Coats, R. S., Elizondo, J. M., LeChien, K. R., Harjes, H. C., Lehr, J. M., Maenchen, J. E. & McDaniel, D. H. (2007, June). An overview of pulse compression and power flow in the upgraded Z pulsed power driver. In *2007 16th IEEE International Pulsed Power Conference* (Vol. 2, pp. 979-984). IEEE.

Seager, S., Kuchner, M., Hier-Majumder, C. A., & Militzer, B. (2007). Mass-radius relationships for solid exoplanets. *The Astrophysical Journal*, *669*(2), 1279.

Seagle, C. T., Davis, J. P., & Knudson, M. D. (2016). Mechanical response of lithium fluoride under off-principal dynamic shock-ramp loading. *Journal of Applied Physics*, *120*(16), 165902.

Seagle, C. T., Davis, J. P., Martin, M. R., & Hanshaw, H. L. (2013). Shock-ramp compression: Ramp compression of shock-melted tin. *Applied Physics Letters*, *102*(24), 244104.

Seagle, C. T., & Porwitzky, A. J. (2018, July). Shock-ramp compression of tin near the melt line. In *AIP Conference Proceedings* (Vol. 1979, No. 1, p. 040005). AIP Publishing LLC.

Sha, X., & Cohen, R. E. (2010). First-principles thermal equation of state and thermoelasticity of hcp Fe at high pressures. *Physical Review B*, *81*(9), 094105.

Sinmyo, R., Hirose, K., & Ohishi, Y. (2019). Melting curve of iron to 290 GPa determined in a resistance-heated diamond-anvil cell. *Earth and Planetary Science Letters*, *510*, 45-52.

Sjostrom, T., & Crockett, S. (2018). Quantum molecular dynamics of warm dense iron and a five-phase equation of state. *Physical Review E*, *97*(5), 053209.

Smith, R. F., Fratanduono, D. E., Braun, D. G., Duffy, T. S., Wicks, J. K., Celliers, P. M., Ali, S. J., Fernandez-Pañella, A., Kraus, R. G., Swift, D. C. & Collins, G. W. (2018). Equation of state of iron under core conditions of large rocky exoplanets. *Nature Astronomy*, *2*(6), 452-458.

Sotin, C., Grasset, O., & Mocquet, A. (2007). Mass–radius curve for extrasolar Earth-like planets and ocean planets. *Icarus*, *191*(1), 337-351.

Soubiran, F., & Militzer, B. (2018). Electrical conductivity and magnetic dynamos in magma oceans of Super-Earths. *Nature communications*, *9*(1), 1-7.

Stacey, F. D., & Davis, P. M. (2008). *Physics of the Earth*. Cambridge University Press.

Stevenson, D. J. (1982). Formation of the giant planets. *Planetary and Space Science*, *30*(8), 755-764.

Swift, D. C., Eggert, J. H., Hicks, D. G., Hamel, S., Caspersen, K., Schwegler, E., Collins, G. W., Nettelmann, N. & Ackland, G. J. (2011). Mass-radius relationships for exoplanets. *The Astrophysical Journal*, *744*(1), 59.

Tange, Y., Nishihara, Y., & Tsuchiya, T. (2009). Unified analyses for P-V-T equation of state of MgO: A solution for pressure-scale problems in high P-T experiments. *Journal of Geophysical Research: Solid Earth*, *114*(B3).

Unterborn, C. T., Dismukes, E. E., & Panero, W. R. (2016). Scaling the Earth: a sensitivity analysis of terrestrial exoplanetary interior models. *The Astrophysical Journal*, *819*(1), 32.

Unterborn, C. T., & Panero, W. R. (2019). The pressure and temperature limits of likely rocky exoplanets. *Journal of Geophysical Research: Planets*, *124*(7), 1704-1716.

Valencia, D., O'Connell, R. J., & Sasselov, D. (2006). Internal structure of massive terrestrial planets. *Icarus*, *181*(2), 545-554.

Valencia, D., O'Connell, R. J., & Sasselov, D. D. (2009). The role of high-pressure experiments on determining super-Earth properties. *Astrophysics and Space Science*, *322*(1-4), 135-139.

Vinet, P., Rose, J. H., Ferrante, J., & Smith, J. R. (1989). Universal features of the equation of state of solids. *Journal of Physics: Condensed Matter*, *1*(11), 1941.

Wagner, F. W., Sohl, F., Hussmann, H., Grott, M., & Rauer, H. (2011). Interior structure models of solid exoplanets using material laws in the infinite pressure limit. *Icarus*, *214*(2), 366-376.

Wang, J., Smith, R. F., Eggert, J. H., Braun, D. G., Boehly, T. R., Reed Patterson, J., Celliers, P. M., Jeanloz, R., Collins, G. W. & Duffy, T. S. (2013). Ramp compression of iron to 273 GPa. *Journal of Applied Physics*, *114*(2), 023513.

Williamson, E. D., & Adams, L. H. (1923). Density distribution in the Earth. *Journal of the Washington Academy of Sciences*, *13*(19), 413-428.

Zapolsky, H. S., & Salpeter, E. E. (1969). The mass-radius relation for cold spheres of low mass. *The Astrophysical Journal*, *158*, 809.

Zel'Dovich, Y. B., & Raizer, Y. P. (2002). *Physics of shock waves and high-temperature hydrodynamic phenomena*. Courier Corporation.

Zeng, L., Sasselov, D. D., & Jacobsen, S. B. (2016). Mass–radius relation for rocky planets based on PREM. *The Astrophysical Journal*, *819*(2), 127.

Zhang, Y., Sekine, T., Lin, J. F., He, H., Liu, F., Zhang, M., Sato, T., Zhu, W. & Yu, Y. (2018). Shock compression and melting of an Fe-Ni-Si alloy: Implications for the temperature profile of the Earth's core and the heat flux across the core-mantle boundary. *Journal of Geophysical Research: Solid Earth*, *123*(2), 1314-1327.